Supplementary Information for:

Dinitrogen Reduction Chemistry with Scandium Provides a Complex with Two Side-on $(N=N)^{2-}$ Ligands Bound to One Metal: $(C_5Me_5)Sc[(\mu\text{-}\eta^2\text{:}\eta^2\text{-}N_2)Sc(C_5Me_5)_2]_2$

Joshua D. Queen,[a] Ahmadreza Rajabi,[a] Quinn E. Goudzwaard,[a] Qiong Yuan,[b] Dang Khoa Nguyen,[a] Joseph W. Ziller,[a] Filipp Furche,*[a] Zhenfeng Xi,*[b] and William J. Evans*[a]

[a] Department of Chemistry, University of California, Irvine, California, 92697

[b] Beijing National Laboratory for Molecular Sciences (BNLMS), Key Laboratory of Bioorganic Chemistry and Molecular Engineering of Ministry of Education, College of Chemistry, Peking University, Beijing 100871, China

Table of Contents

Experimental Details

General Considerations. All manipulations were performed by using modified Schlenk techniques or in a Vacuum/Atmospheres glovebox under nitrogen or argon. Solvents were degassed by sparging with dry agon before drying and collection using an S2 Grubbs-type solvent purification system[1] (JC Meyer or MBraun). All physical measurements were recorded under strictly anaerobic and anhydrous conditions. Infrared spectra were recorded on compressed solid samples using an Agilent Cary 630 ATR/FTIR instrument. Electronic spectra were recorded as dilute solutions in the indicated solvent in quartz cuvettes (1 mm path length) using an Agilent Cary 60 UV/vis spectrophotometer. Combustion analyses were performed using a Thermo Scientific FlashSmart CHNS/O Elemental Analyzer at the UC Irvine Materials Research Institute's TEMPR facility. NMR spectra were recorded using Bruker AVANCE 600 MHz, 500 MHz, or 400 MHz NMR spectrometers and referenced to residual solvent signals[2] for ^{1}H and $^{13}C\{^{1}H\}$. $^{15}N\{^{1}H\}$ NMR spectra were calibrated using an external reference, neat nitromethane at 0 ppm. Magnetic moments were determined by Evans' method and corrected using the appropriate diamagnetic constants.[3-5] Raman spectra of **1** and **3** were recorded using a Renishaw inVia Raman microscope on solid samples that were flame sealed in 1 mm capillary tubes under inert atmosphere and taped to a microscope slide. Raman spectra of **2** and **^{15}N-2** were collected on crystalline samples sealed in J. Young valve NMR tubes using a Thermo Scientific DXRxi Raman Imaging Microscope. KCp*,[6] KC_8,[7] and Cp^*_2ScI[8,9] were prepared according to the literature methods. Cp^*_2ScCl and $Cp^*_2ScCl(THF)$ were prepared as described by modifications of literature methods.[8,10]

$(Cp^*_2Sc)_2(\mu\text{-}\eta^1\text{:}\eta^1\text{-}N_2)$, 1. Inside a nitrogen filled glovebox, KC_8 (0.134 g, 0.991 mmol) was added to a stirred yellow solution of Cp^*_2ScI (0.400 g, 0.905 mmol) in ca. 15 mL of Et_2O.

The mixture immediately became dark blue and was stirred overnight. The mixture was centrifuged and the supernatant filtered through a pipette packed with Kimwipes. The remaining solids were extracted with ca. 10 mL of Et_2O, centrifuged, and filtered. This was process was done 8 times after which no blue material remained and the extracted solution was colorless. The combined supernatants were evaporated to dryness to give **1** as a dark blue powder (0.240 g, 0.364 mmol, 81%). A 2 mL portion of a saturated solution of **1** in Et_2O was filtered and stored at −35°C to give several highly air sensitive X-ray quality crystals of **1**. M.P. 183–187°C (dec). The dark blue solid turns red upon melting with gas evolution before turning colorless. Anal. Calcd for $C_{40}H_{60}N_2Sc_2$: C, 72.92; H, 9.18; N, 4.25. Found: C, 71.99; H, 9.15; N, 4.08. ^{1}H NMR (500 MHz, C_6D_6, 298 K): δ 29.2 (br, $\Delta\nu_{½}$ = 210 Hz, 60 H, *Cp**). Magnetic moment (Evans' method, C_6D_6): 2.8 μB. UV-visible (ε = L mol^{-1} cm^{-1}): 353 nm (15000), 600 nm (20000). ATR-FTIR (cm^{-1}): 2897s, 2853s, 2721w, 1486w, 1433s, 1378s, 1242w, 1151w, 1121w, 1063w, 1021m, 957w, 859w, 830w, 800w, 745w. Raman shift: 1595 cm^{-1}.

Cp*Sc[(μ-η^2:η^2-N$_2$)ScCp*$_2$]$_2$, 2. Method A. Inside a nitrogen filled glovebox, KC_8 (0.14 g, 0.106 mmol) was added in one portion to a stirred solution of **1** (0.100 g, 0.152 mmol) in ca. 10 mL of Et_2O and stirred for 15 min during which time the color changed from dark blue to orange. The solvent was removed under reduced pressure and the residue was extracted twice with ca. 4 mL hexane, centrifuged, and the supernatant filtered through a pipette packed with Kimwipes. The solution was concentrated to ca. 2 mL and stored at −35°C to give brown crystals of **2** (0.063 g, 0.073 mmol, 72%). M.P. 188–193°C (dec). Anal. Calcd for $C_{50}H_{75}N_4Sc_3$: C, 69.26; H, 8.72; N, 6.46. Found: C, 69.60; H, 8.71; N, 6.23. ^{1}H NMR (500 MHz, C_6D_6, 298 K): 2.26 (s, 15 H, Sc(C_5*Me$_5$*)), 1.87 (s, 60 H, Sc(C_5*Me$_5$*)$_2$). ^{13}C NMR (151 MHz, C_6D_6, 298 K): 119.92 (Sc(*C*$_5$Me$_5$)), 117.52(Sc(*C*$_5$Me$_5$)$_2$), 12.31 (Sc(C_5*Me$_5$*)), 11.40 (Sc(C_5*Me$_5$*)$_2$). UV-visible (ε = L mol^{-1} cm^{-1}): 430

nm, shoulder (2300), 510 nm, shoulder (1000), 656 nm (400), 780 nm (300). ATR-FTIR (cm^{-1}): 2901s, 2854s, 2721w, 1491w, 1434s, 1376s, 1257w, 1243w, 1149m, 1099w, 1060m, 1020m, 958w, 885w, 801w, 754s, 654s. Raman shift: 1460 cm^{-1}.

Method B. Inside a nitrogen filled glovebox, KC_8 (0.130 g 0.962 mmol) was added in one portion to a stirred solution of Cp^*_2ScI (0.260 g, 0.589 mmol) in ca. 10 mL of Et_2O resulting in an immediate color change from yellow to dark blue. The mixture was stirred 3 hours after which the color had become dark orange. The solvent was removed by vacuum and the solids extracted 3 times with ca. 6 mL of hexanes. The combined supernatants were centrifuged, filtered through a pipette packed with Kimwipes, concentrated to ca. 3 mL, and stored at −35°C to afford brown crystals of **2** (0.134 g, 0.155 mmol, 79%).

Method C. Inside a nitrogen-filled glovebox, KC_8 (0.176 g, 1.31 mmol) was added to a mixture of Cp^*_2ScCl (0.114 g, 0.326 mmol) and $Cp^*_2ScCl(THF)$ (0.275 g, 0.651 mmol) in ca. 10 mL of toluene. After stirring for 15 min, the solution turned to dark blue. The mixture was stirred for 12 hours, after which the color had become dark orange. The solvent was removed under vacuum, and the solids were extracted three times with ca. 6 mL of hexanes. After filtration, the solution was concentrated to ca. 3 mL and stored at −35°C to afford brown crystals of **2** (0.229 g, 0.264 mmol, 81%).

$Cp^*Sc[(\mu\text{-}\eta^2\text{:}\eta^2\text{-}{}^{15}N_2)ScCp^*_2]_2$, ^{15}N-2: In an argon atmosphere, **Cp^*_2ScCl** (0.0521 g, 0.148 mmol), **$Cp^*_2ScCl(THF)$** (0.1256 g, 0.297 mmol), and KC_8 (0.0801 g, 0.594 mol) were mixed in a Schlenk reaction tube, followed by the addition of 5 mL of toluene. The reaction mixture was frozen, and the argon was removed under vacuum, after which $^{15}N_2$ gas was introduced into the system. The reaction was allowed to proceed at room temperature for 18 hours. The method for obtaining crystals of **^{15}N-2** was similar to that used for **2**, with all procedures

conducted under an argon atmosphere. Specifically, in an argon atmosphere, the solvent was removed by vacuum, and the solids were extracted three times with ca. 6 mL hexanes. After filtration, the solution was concentrated to ca. 3 mL and stored at −35 °C to afford brown crystals of **^{15}N-2** (0.083 g, 0.096 mmol, 65%). Raman shift: 1415 cm^{-1}.

$Cp^*_2Sc(\mu\text{-}\eta^2\text{:}\eta^2\text{-}N_2)ScI(THF)Cp^*$, 3. Inside a nitrogen filled glovebox, KC_8 (0.060 g) was added a to a solution of Cp^*_2ScI (0.200 g) and 18-crown-6 (0.120 g) in Et_2O (10 mL). The mixture was stirred for 20 min, during which time it change from yellow to dark blue to orange. The mixture was centrifuged and the orange supernatant filtered through a pipette packed with Kimwipes. The solvent was removed under reduced pressure to give **2** as an orange powder (0.096 g, 74% based on Cp^*_2ScI). The residual green-black solids from the reaction were mixed with ca. 4 mL of THF and then the solvent removed under vacuum. The residue was then extracted twice with 5 mL portions of hexane. The resulting green solution was centrifuged and filtered through a pipette packed with 1 cm Kimwipes. The solvent was removed under vacuum to give 15 mg (9% based on Cp^*_2ScI) of crude **3** as a pale green powder which was determined to be ca. 50% pure by ^{1}H NMR spectroscopy. Recrystallization from *n*-hexane at −35°C gave green blocks suitable for X-ray crystallography. ^{1}H NMR (500 MHz, C_6D_6, 298 K): 4.26-4.19 (br, 4H, $O(CH_2CH_2)_2$), 2.29 (s, 15H, Sc*Cp**I), 1.80 (s, 30 H, Sc*Cp*$^*_2$), 1.40 (br, 4H, $O(CH_2CH_2)_2$, overlapping with free THF). UV-visible (ε = L mol^{-1} cm^{-1}): 616 nm (70). ATR-FTIR (cm^{-1}): 2900s, 2858s, 2752w, 1491w, 1434s, 1377(s). 1351w, 1294w, 1248w, 1106s, 1060w, 1012s, 961m, 859m, 838m, 804w, 746m, 671w. Raman shift: 1700 cm^{-1}.

$(Cp^*Sc)_4(\mu_4\text{-}O)(\mu\text{-}OH)_6$, 4. A solution of **1** (0.015 g) in *ca*. 3 mL of *n*-hexane was stirred inside an argon filled glovebox overnight and became colorless. The solvent was removed and the residue was dissolved in C_6D_6, showing a signal at 2.01 ppm. The sample was brought back into

the glovebox and slowly evaporated overnight yielding several colorless blocks of **4** which did not redissolve in C_6D_6.

Synthesis of Cp*$_2$ScCl(THF). $ScCl_3$ (0.303 g, 2.00 mmol) was added to ca.15 mL THF, heated to 70 ℃ and solvated for over 4 hours. Then, the THF suspension of KCp* (0.701 g, 4.00 mmol) was added. The mixture was stirred 12 hours at room temperature to obtain yellow turbid liquid. The solvent was removed by vacuum, and the solids were extracted three times with ca. 10 mL toluene. After filtration, concentrated to ca. 10 mL and stored at −35°C to afford yellow crystals of **Cp*$_2$ScCl(THF)**. (Yield: 0.550 g, 1.30 mmol 65 %). ^{1}H NMR (400 MHz, d^8-toluene**)** δ 1.31-1.27(4H, CH_2CH_2) 1.88 (s, 30H, Me_5C_5) 3.55-3.52 (4H, CH_2CH_2)

Synthesis of Cp*$_2$ScCl. Dissolve $ScCl_3$ (0.303 g, 2.00 mmol,) and KCp* (0.701 g, 4 mmol,) in ca. 40 mL of toluene, heat to 100 ℃, and react for 72 hours to obtain yellow turbid liquid. The solvent was removed by vacuum, and the solids were extracted three times with ca. 10 mL hexanes. The combined supernatants were filtered and concentrated to ca. 10 mL, and stored at −35°C to afford yellow crystals of **Cp*$_2$ScCl**. **(**Yield: 0.561 g, 1.60 mmol 80 %). ^{1}H NMR (400 MHz, d^8-toluene**)** δ 1.88 (s, 30H, Me_5C_5).

The reaction of 1 with N_2O: A solution of **1** (ca. 5 mg) in C_6D_6 (ca. 0.5 mL) inside a J. Young NMR tube was placed under an atmosphere of N_2O resulting in a rapid color change from dark blue to pale yellow. The broad ^{1}H NMR signal at 29 ppm corresponding to **1** was replaced by a sharp singlet at 2.01 ppm.

The reaction of 2 with N_2O: A solution of **2** (ca. 5 mg) in C_6D_6 (ca. 0.5 mL) inside a J. Young NMR tube was placed under an atmosphere of N_2O resulting in a rapid color change from orange to pale green to colorless. The ^{1}H NMR signals corresponding to **2** at 2.26 ppm and 1.87 ppm were replaced by new signals at 2.26 ppm (s, 15 H) and 2.03 ppm (s, 60 H).

Xray Crystallography

X-ray Data Collection, Structure Solution and Refinement for 1.

A purple crystal of approximate dimensions 0.225 x 0.178 x 0.096 mm was mounted in a cryoloop and transferred to a Bruker SMART APEX II diffractometer system. The APEX2[11] program package was used to determine the unit-cell parameters and for data collection (120 sec/frame scan time). The raw frame data was processed using SAINT[12] and SADABS[13] to yield the reflection data file. Subsequent calculations were carried out using the SHELXTL[14] program package. The diffraction symmetry was *mmm* and the systematic absences were consistent with the orthorhombic space group *I*222 that was later determined to be correct.

The structure was solved by direct methods and refined on F^2 by full-matrix least-squares techniques. The analytical scattering factors[15] for neutral atoms were used throughout the analysis.

Hydrogen atoms were included using a riding model. Disordered scandium atoms consisting of 5% occupancy were refined isotropically. Least squares analysis yielded wR2 = 0.1132 and Goof = 1.058 for 109 variables refined against 2836 data (0.74 Å), R1 = 0.0458 for those 2511 data with $I > 2.0\sigma(I)$. The absolute structure was assigned by refinement of the Flack parameter[16].

X-ray Data Collection, Structure Solution and Refinement for 2.

A brown crystal of approximate dimensions 0.372 x 0.188 x 0.052 mm was mounted in a cryoloop and transferred to a Bruker SMART APEX II diffractometer system. The APEX2[11] program package was used to determine the unit-cell parameters and for data collection (120 sec/frame scan time). The raw frame data was processed using SAINT[12] and SADABS[13] to yield the reflection data file. Subsequent calculations were carried out using the SHELXTL[14] program

package. The diffraction symmetry was 2/*m* and the systematic absences were consistent with the monoclinic space groups *Cc* and *C*2/*c*. It was later determined that space group *C*2/*c* was correct.

The structure was solved by direct methods and refined on F^2 by full-matrix least-squares techniques. The analytical scattering factors[15] for neutral atoms were used throughout the analysis.

Hydrogen atoms were included using a riding model.

Least-squares analysis yielded wR2 = 0.1226 and Goof = 1.025 for 539 variables refined against 14552 data (0.70 Å), R1 = 0.0446 for those 10089 data with $I > 2.0\sigma(I)$.

X-ray Data Collection, Structure Solution and Refinement for 3.

A green crystal of approximate dimensions 0.294 x 0.205 x 0.188 mm was mounted in a cryoloop and transferred to a Bruker SMART APEX II diffractometer system. The APEX2[11] program package was used to determine the unit-cell parameters and for data collection (30 sec/frame scan time). The raw frame data was processed using SAINT[12] and SADABS[13] to yield the reflection data file. Subsequent calculations were carried out using the SHELXTL[14] program package. The diffraction symmetry was *mmm* and the systematic absences were consistent with the orthorhombic space group $P2_12_12_1$ that was later determined to be correct.

The structure was solved by direct methods and refined on F^2 by full-matrix least-squares techniques. The analytical scattering factors[15] for neutral atoms were used throughout the analysis.

Hydrogen atoms were included using a riding model. Crystallographic disorder of the scandium and nitrogen atoms related to side-on and end-on isomerization was modeled as 82% consisting of the side-on isomer and 12% the end-on isomer. Nitrogen atoms of the end-on isomer were refined isotropically.

Least squares analysis yielded wR2 = 0.0889 and Goof = 1.073 for 458 variables refined against 1259 data (0.70 Å), R1 = 0.0327 for those 11609 data with I > 2.0σ(I). The absolute structure was assigned by refinement of the Flack parameter.[16]

X-ray Data Collection, Structure Solution and Refinement for 4.

A colorless crystal of approximate dimensions 0.389 x 0.343 x 0.122 mm was mounted in a and transferred to a Bruker SMART APEX II diffractometer system. The APEX3[17] program package was used to determine the unit-cell parameters and for data collection (10-30 sec/frame scan time). The raw frame data was processed using SAINT[12] and SADABS[13] to yield the reflection data file. Subsequent calculations were carried out using the SHELXTL[14] program package. There were no systematic absences nor any diffraction symmetry other than the Friedel condition. The centrosymmetric triclinic space group $P\bar{1}$ was assigned and later determined to be correct.

The structure was solved by direct methods and refined on F^2 by full-matrix least-squares techniques. The analytical scattering factors[5] for neutral atoms were used throughout the analysis. Hydrogen atoms were included using a riding model.

Least-squares analysis yielded wR2 = 0.1212 and Goof = 1.084 for 504 variables refined against 8066 data (0.83 Å), R1 = 0.0496 for those 7290 data with I > 2.0σ(I).

Structural Discussion of $(Cp^*Sc)_4(\mu_4\text{-}O)(\mu\text{-}OH)_6$, 4.

Compound **4** has a diamondoid core, Figure S1 consisting of four scandium atoms bridged by six hydroxide groups. The scandium atoms form a regular tetrahedron with ca. 3.33Å Sc···Sc separations and a central μ_4-oxide ligand which has Sc-O distances in the narrow range of 2.029(2)-2.046(2) Å. The Sc-O distances of the bridging hydroxyl groups all lie in the range

2.087(2)-2.11(4) Å and the Sc-Cp*(centroid) distances show only slight variation between 2.20-2.22 Å. These values are summarized in Table S1.

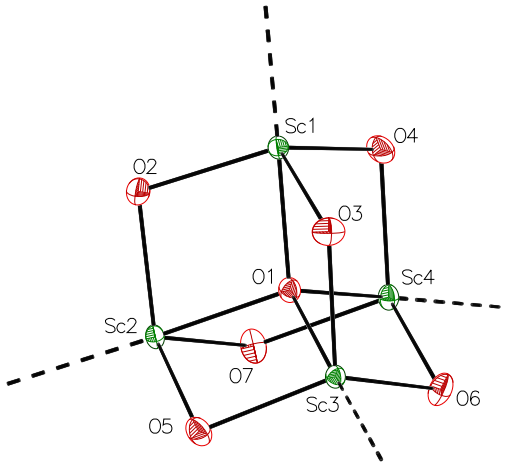

Figure S1. Molecular structure of the Sc_4O_7 core of **4**. Hydrogen atoms and Cp* ligands not shown for clarity.

Table S1. Selected bond length parameters (Å) for **4**.

Sc1-O1	2.0455(19)	**Sc2-O1**	2.0402(19)	**Sc3-O1**	2.0423(19)	**Sc4-O1**	2.0292(18)
Sc1-O2	2.093(2)	**Sc3-O5**	2.100(2)	**Sc3-O3**	2.097(2)	**Sc4-O4**	2.094(2)
Sc1-O3	2.093(2)	**Sc3-O6**	2.087(2)	**Sc3-O5**	2.100(2)	**Sc4-O6**	2.114(2)
Sc1-O4	2.100(2)	**Sc4-O4**	2.094(2)	**Sc3-O6**	2.087(2)	**Sc4-O7**	2.093(2)
Sc1-Cent	2.20	**Sc2-Cent**	2.21	**Sc3-Cent**	2.22	**Sc4-Cent**	2.21

Structural Discussion of Cp^*_2ScCl and $Cp^*_2ScCl(THF)$.

The structure of Cp^*_2ScCl[8] has been obtained previously by Conley and coworkers in the monoclinic space group $P2_1$ with four independent molecules in the asymmetric unit.[9] Recrystallization from hexanes as described above gave crystals of Cp^*_2ScCl, Figure S2, left, in the orthorhombic space group $P2_12_12_1$ with only one crystallographically independent molecule. When THF instead of toluene was used as the reaction solvent, crystals of the THF complex $Cp^*_2ScCl(THF)$, Figure S2, right, were obtained which has two crystallographically independent molecules in the asymmetric unit. This complex had previously been prepared by Conley and coworkers, but was not crystallographically characterized.[9]

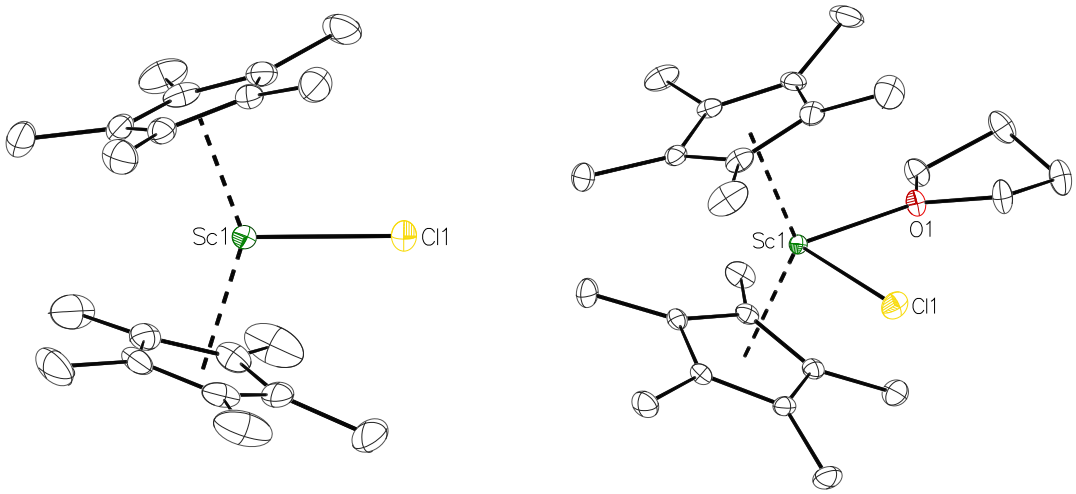

Figure S2 Molecular structures of **Cp^*_2ScCl** (left) and **$Cp^*_2ScCl(THF)$** (right) with ellipsoids shown at 30% probability and H atoms not shown for clarity

As shown in Table S2, the structural parameters of Cp^*_2ScCl are close to the average values reported by Conley and coworkers. Upon coordination of THF, the Sc-Cl is lengthened by almost 0.04 Å to ca. 2.45 Å while the Sc-Cp*(centroid) distances are lengthened by approximately 0.08 Å to 2.24 and 2.25 Å. The 142.8° Cp*(centroid)-Sc-Cp*(centroid) angle in Cp^*_2ScCl decreased

to ca. 137° in the higher coordinate $Cp^*_2ScCl(THF)$. The THF molecules coordinate the Sc atom at near right angles to the Cl ligand with O-Sc-Cl angles of 88.65(3) and 89.75(3)° and the Sc-O distances show more variability than the other ligands being 2.259(1) and 2.2805(9) Å in the two different molecules.

Table S2. Selected metrical parameters of Cp^*_2ScCl and $Cp^*_2ScCl(THF)$

	Cp^*_2ScCl ($P2_1$)[a]	**Cp^*_2ScCl ($P2_12_12_1$)[b]**	**$Cp^*_2ScCl(THF)$[b]**
Sc-Cl (Å)	2.418(2)	2.412(1)	2.4576(5), 2.4546(5)
Sc-Cent (Å)	2.15, 2.16	2.16, 2.16	2.24, 2.25
Sc-O (Å)	—	—	2.259(1), 2.2805(9)
Cent-Sc-Cent (°)	142.71	142.8	136.3, 137.5
Cent-Sc-Cl (°)	108.6, 109.5	108.6, 108.6	106.1, 105.7, 105.9, 105.4
Cent-Sc-O (°)	—	—	104.5, 105.4, 104.3, 104.3
O-Sc-Cl (°)	—	—	88.65(3), 89.75(3)

[a]Average values, ref 9.
[b]This work

Table S3. Crystal data and structure refinement for **1**.

Empirical formula	$C_{40}H_{60}N_2Sc_2$	
Formula weight	658.82	
Temperature	133(2) K	
Wavelength	0.71073 Å	
Crystal system	Orthorhombic	
Space group	*I*222	
Unit cell dimensions	a = 10.9904(15) Å	α = 90°
	b = 11.3937(16) Å	β = 90°
	c = 14.908(2) Å	γ = 90°
Volume	1866.8(4) $Å^3$	
Z	2	
Density (calculated)	1.172 Mg/m^3	
Absorption coefficient	0.392 mm^{-1}	
F(000)	712	
Crystal color	purple	
Crystal habit	block	
Crystal size	0.225 × 0.178 × 0.096 mm^3	
Theta range for data collection	2.250 to 30.538°.	
Index ranges	$-15 \leq h \leq 15$, $-16 \leq k \leq 15$, $-21 \leq l \leq 21$	
Reflections collected	22932	
Independent reflections	2836 [R(int) = 0.0787]	
Completeness to theta = 25.242∞	100.0 %	
Absorption correction	Semi-empirical from equivalents	
Max. and min. transmission	0.746 and 0.610	
Refinement method	Full-matrix least-squares on F^2	
Data / restraints / parameters	2836 / 0 / 109	
Goodness-of-fit on F^2	1.058	
Final R indices [I>2sigma(I)]	R1 = 0.0458, wR2 = 0.1071	
R indices (all data)	R1 = 0.0563, wR2 = 0.1123	
Absolute structure parameter	0.14(5)	
Largest diff. peak and hole	0.494 and -0.396 e $Å^{-3}$	

Table S4. Crystal data and structure refinement for **2**.

Empirical formula	$C_{50}H_{75}N_4Sc_3$	
Formula weight	867.02	
Temperature	183(2) K	
Wavelength	0.71073 Å	
Crystal system	Monoclinic	
Space group	*C*2/*c*	
Unit cell dimensions	a = 43.206(8) Å	α= 90°
	b = 9.8953(19) Å	β= 119.166(3)°
	c = 25.757(5) Å	γ = 90°
Volume	9616(3) $Å^3$	
Z	8	
Density (calculated)	1.198 Mg/m^3	
Absorption coefficient	0.448 mm^{-1}	
F(000)	3728	
Crystal size	0.372 × 0.188 × 0.052 mm^3	
Theta range for data collection	1.079 to 30.640°.	
Index ranges	$-59 \le h \le 61$, $-14 \le k \le 14$, $-36 \le l \le 36$	
Reflections collected	117494	
Independent reflections	14552 [R(int) = 0.0713]	
Completeness to theta = 25.242°	100.0 %	
Absorption correction	Semi-empirical from equivalents	
Max. and min. transmission	0.8724 and 0.7893	
Refinement method	Full-matrix least-squares on F^2	
Data / restraints / parameters	14552 / 0 / 539	
Goodness-of-fit on F^2	1.026	
Final R indices [I>2sigma(I)]	R1 = 0.0446, wR2 = 0.1063	
R indices (all data)	R1 = 0.0802, wR2 = 0.1226	
Largest diff. peak and hole	0.516 and -0.305 e.$Å^{-3}$	

Table S5. Crystal data and structure refinement for **3**.

Empirical formula	$C_{40}H_{67}N_2OSc_2I$	
Formula weight	808.77	
Temperature	93(2) K	
Wavelength	0.71073 Å	
Crystal system	Orthorhombic	
Space group	$P2_12_12_1$	
Unit cell dimensions	a = 13.4651(9) Å	α= 90°
	b = 14.9197(10) Å	β= 90°
	c = 20.5495(13) Å	γ = 90°
Volume	4128.3(5) $Å^3$	
Z	4	
Density (calculated)	1.301 Mg/m^3	
Absorption coefficient	1.107 mm^{-1}	
F(000)	1696	
Crystal size	0.294 × 0.205 × 0.188 mm^3	
Theta range for data collection	1.808 to 30.624°.	
Index ranges	$-19 \le h \le 19$, $-21 \le k \le 21$, $-29 \le l \le 29$	
Reflections collected	66705	
Independent reflections	12559 [R(int) = 0.0415]	
Completeness to theta = 25.242°	100.0 %	
Absorption correction	Semi-empirical from equivalents	
Max. and min. transmission	0.7461 and 0.5910	
Refinement method	Full-matrix least-squares on F^2	
Data / restraints / parameters	12559 / 0 / 458	
Goodness-of-fit on F^2	1.073	
Final R indices [I>2sigma(I)]	R1 = 0.0327, wR2 = 0.0869	
R indices (all data)	R1 = 0.0366, wR2 = 0.0889	
Absolute structure parameter	0.012(5)	
Largest diff. peak and hole	1.094 and -0.431 $e.Å^{-3}$	

Table S6. Crystal data and structure refinement for **4**.

Empirical formula	$C_{40}H_{66}O_7Sc_4$	
Formula weight	838.76	
Temperature	93(2) K	
Wavelength	1.54178 Å	
Crystal system	Triclinic	
Space group	*P*-1	
Unit cell dimensions	a = 11.5010(9) Å	α= 82.260(4)°
	b = 11.5790(9) Å	β= 81.730(4)°
	c = 18.9570(15) Å	γ = 64.750(3)
Volume	2252.0(3) $Å^3$	
Z	2	
Density (calculated)	1.237 Mg/m^3	
Absorption coefficient	5.308 mm^{-1}	
F(000)	892	
Crystal size	0.389 × 0.343 × 0.122 mm^3	
Theta range for data collection	2.363 to 68.436°	
Index ranges	$-13 \leq h \leq 13$, $-13 \leq k \leq 13$, $-22 \leq l \leq 22$	
Reflections collected	53930	
Independent reflections	8066 [R(int) = 0.0681]	
Completeness to theta = 67.679°	98.5 %	
Absorption correction	Semi-empirical from equivalents	
Max. and min. transmission	0.7531 and 0.5559	
Refinement method	Full-matrix least-squares on F^2	
Data / restraints / parameters	8066 / 0 / 504	
Goodness-of-fit on F^2	1.084	
Final R indices [I>2sigma(I)]	R1 = 0.0469, wR2 = 0.1163	
R indices (all data)	R1 = 0.0523, wR2 = 0.1212	
Largest diff. peak and hole	0.911 and -0.358 $e.Å^{-3}$	

Table S7. Crystal data and structure refinement for Cp^*_2ScCl.

Empirical formula	$C_{20}H_{30}ClSc$	
Formula weight	350.85	
Temperature	179.99(10) K	
Wavelength	0.71073 Å	
Crystal system	Orthorhombic	
Space group	$P2_12_12_1$	
Unit cell dimensions	a = 8.3930(5) Å	α= 90°
	b = 11.1477(7) Å	β= 90°
	c = 20.9045(11) Å	γ = 90°
Volume	1955.9(2) $Å^3$	
Z	4	
Density (calculated)	1.191 Mg/m^3	
Absorption coefficient	0.509 mm^{-1}	
F(000)	752	
Crystal size	0.2 x 0.1 x 0.1 mm^3	
Theta range for data collection	2.070 to 29.890°.	
Index ranges	$-11 \le h \le 11$, $-15 \le k \le 11$, $-24 \le l \le 29$	
Reflections collected	11658	
Independent reflections	4703 [R(int) = 0.0268]	
Completeness to theta = 25.242°	99.9 %	
Absorption correction	Semi-empirical from equivalents	
Max. and min. transmission	1.00000 and 0.96027	
Refinement method	Full-matrix least-squares on F^2	
Data / restraints / parameters	4703 / 0 / 209	
Goodness-of-fit on F^2	1.051	
Final R indices [I>2sigma(I)]	R1 = 0.0407, wR2 = 0.1023	
R indices (all data)	R1 = 0.0484, wR2 = 0.1063	
Absolute structure parameter	0.017(15)	
Largest diff. peak and hole	0.404 and -0.353 $e.Å^{-3}$	

Table S8. Crystal data and structure refinement for $Cp^*_2ScCl(thf)$.

Empirical formula	$C_{24}H_{38}OClSc$	
Formula weight	422.95	
Temperature	179.99(10) K	
Wavelength	0.71073 Å	
Crystal system	Triclinic	
Space group	*P*-1	
Unit cell dimensions	a = 8.4652(3) Å	α= 63.797(3)°
	b = 16.6864(5) Å	β= 88.175(2)°
	c = 17.8292(6) Å	γ = 87.697(2)°
Volume	2257.53(14) $Å^3$	
Z	4	
Density (calculated)	1.244 Mg/m^3	
Absorption coefficient	0.455 mm^{-1}	
F(000)	912	
Crystal size	0.2 x 0.1 x 0.1 mm^3	
Theta range for data collection	2.236 to 30.136°.	
Index ranges	$-11 \leq h \leq 11$, $-22 \leq k \leq 22$, $-24 \leq l \leq 19$	
Reflections collected	46095	
Independent reflections	11733 [R(int) = 0.0315]	
Completeness to theta = 25.242°	99.9 %	
Absorption correction	Semi-empirical from equivalents	
Max. and min. transmission	1.00000 and 0.77096	
Refinement method	Full-matrix least-squares on F^2	
Data / restraints / parameters	11733 / 0 / 508	
Goodness-of-fit on F^2	1.087	
Final R indices [I>2sigma(I)]	R1 = 0.0376, wR2 = 0.0950	
R indices (all data)	R1 = 0.0483, wR2 = 0.1000	
Extinction coefficient	0.0090(7)	
Largest diff. peak and hole	0.471 and -0.368 $e.Å^{-3}$	

NMR Spectra

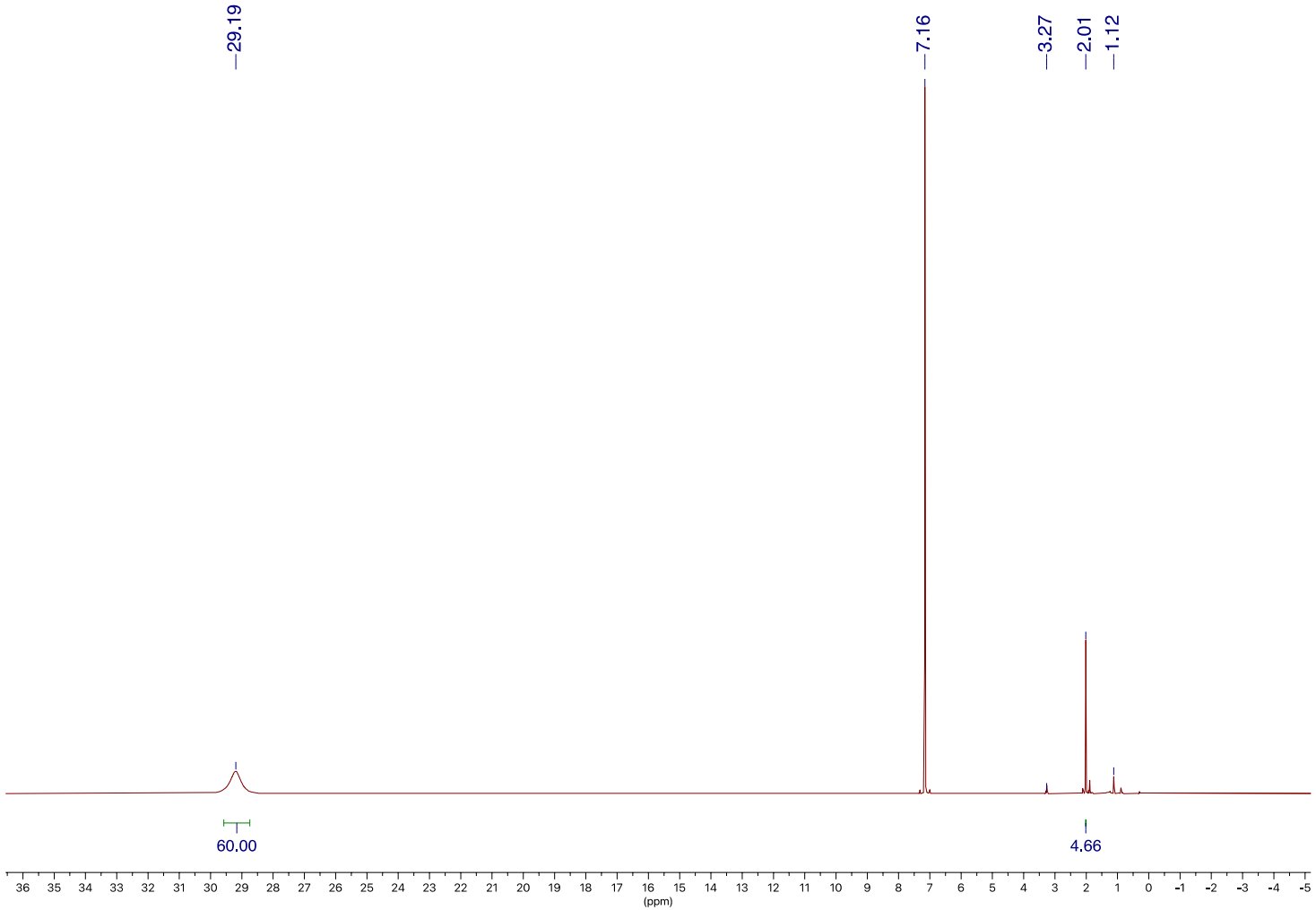

Figure S3. ^{1}H NMR spectrum of $(Cp^*_2Sc)_2(\mu\text{-}\eta^1\text{:}\eta^1\text{-}N_2)$, **1**. The signal at 2.01 is assigned as the possible oxide impurity $(Cp^*_2Sc)_2(\mu\text{-}O)$. 500 MHz, C_6D_6, 298 K.

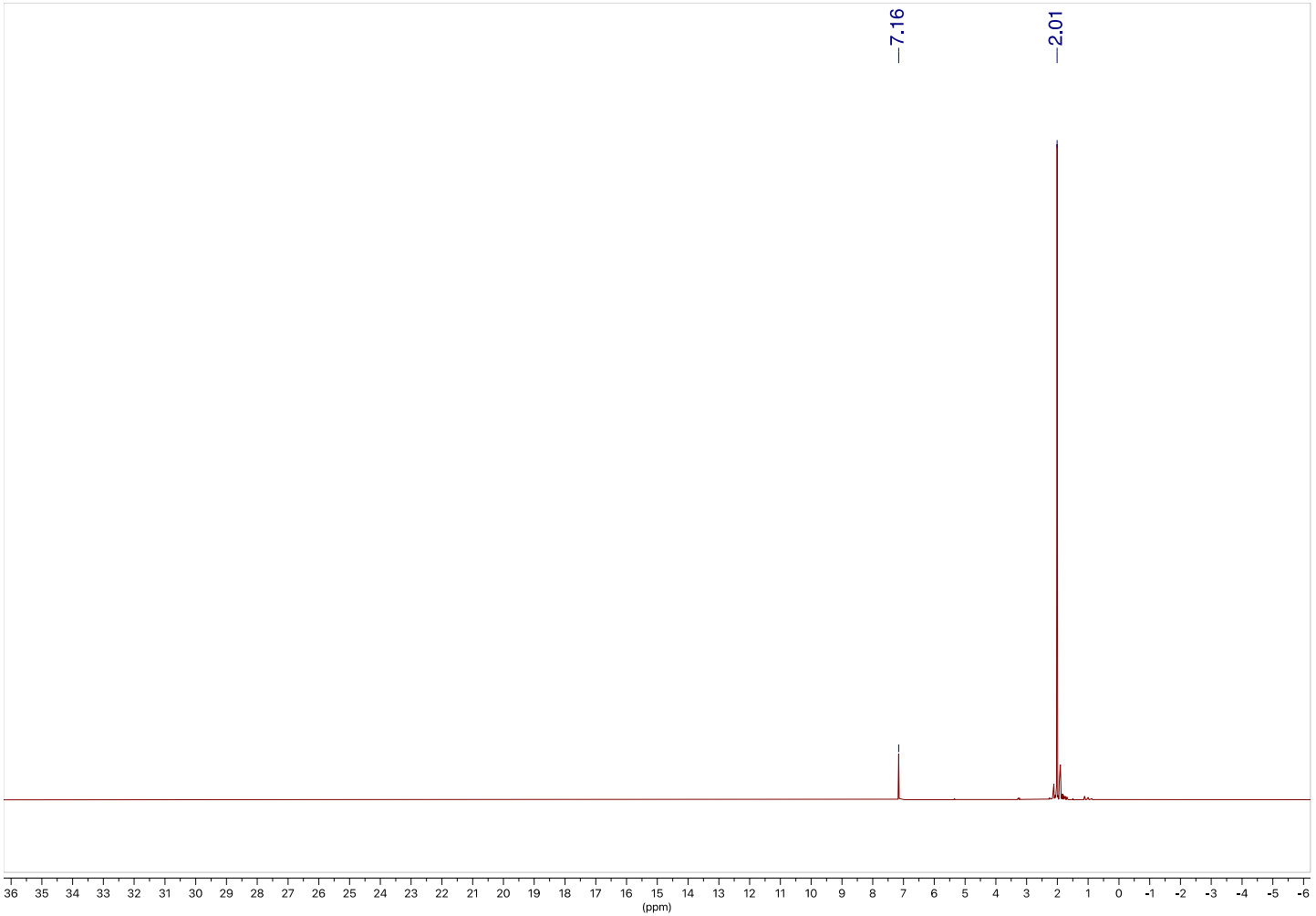

Figure S4. ^{1}H NMR spectrum of the reaction product between $(Cp^*_2Sc)_2(\mu\text{-}\eta^1\text{:}\eta^1\text{-}N_2)$, **1**, and N_2O, presumably $(Cp^*_2Sc)_2(\mu\text{-}O)$. 500 MHz, C_6D_6, 298 K.

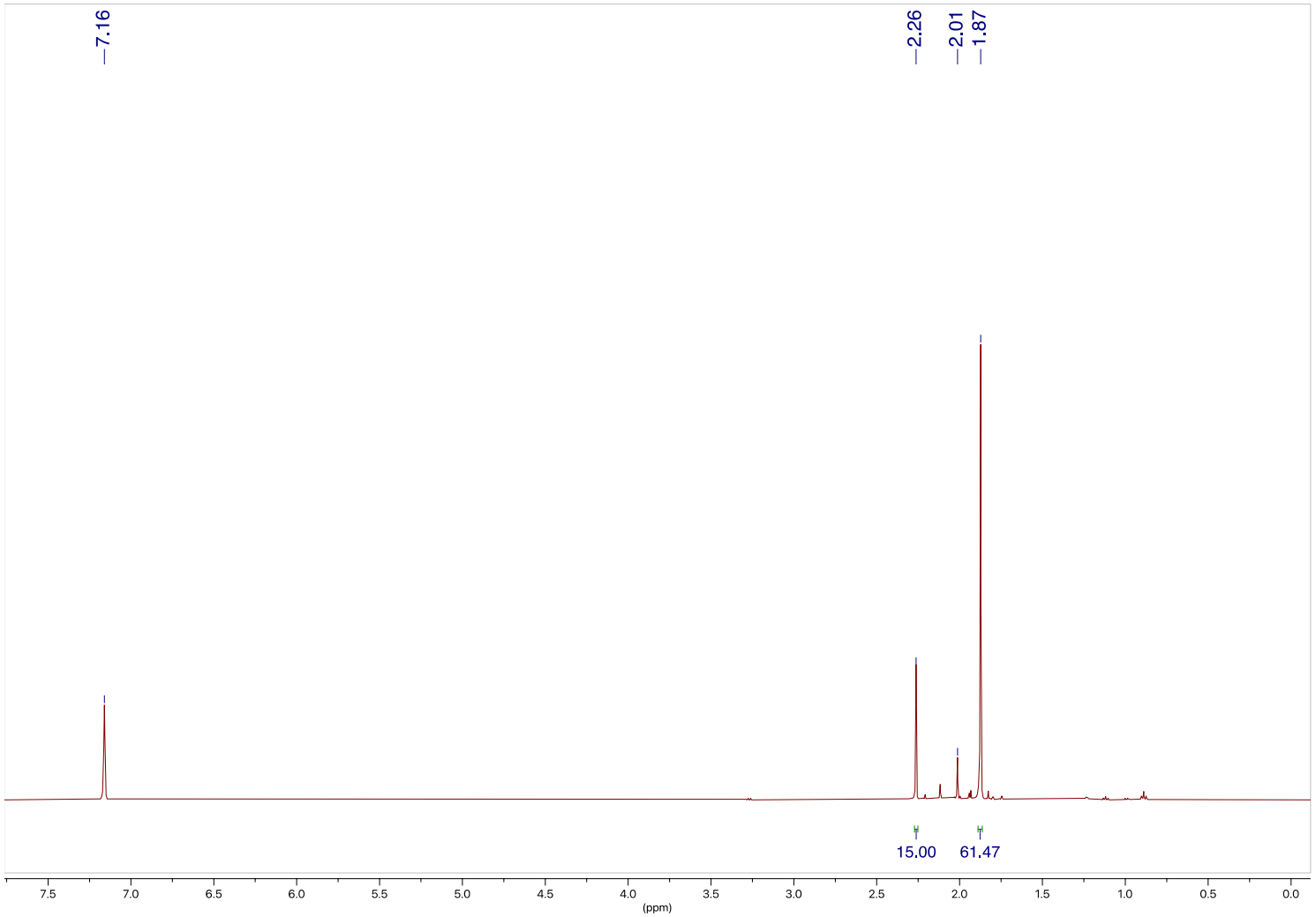

Figure S5. ^{1}H NMR spectrum of Cp*Sc[(μ-η^{2}:η^{2}-N_2)ScCp*$_2$]$_2$. 500 MHz, C_6D_6, 298 K.

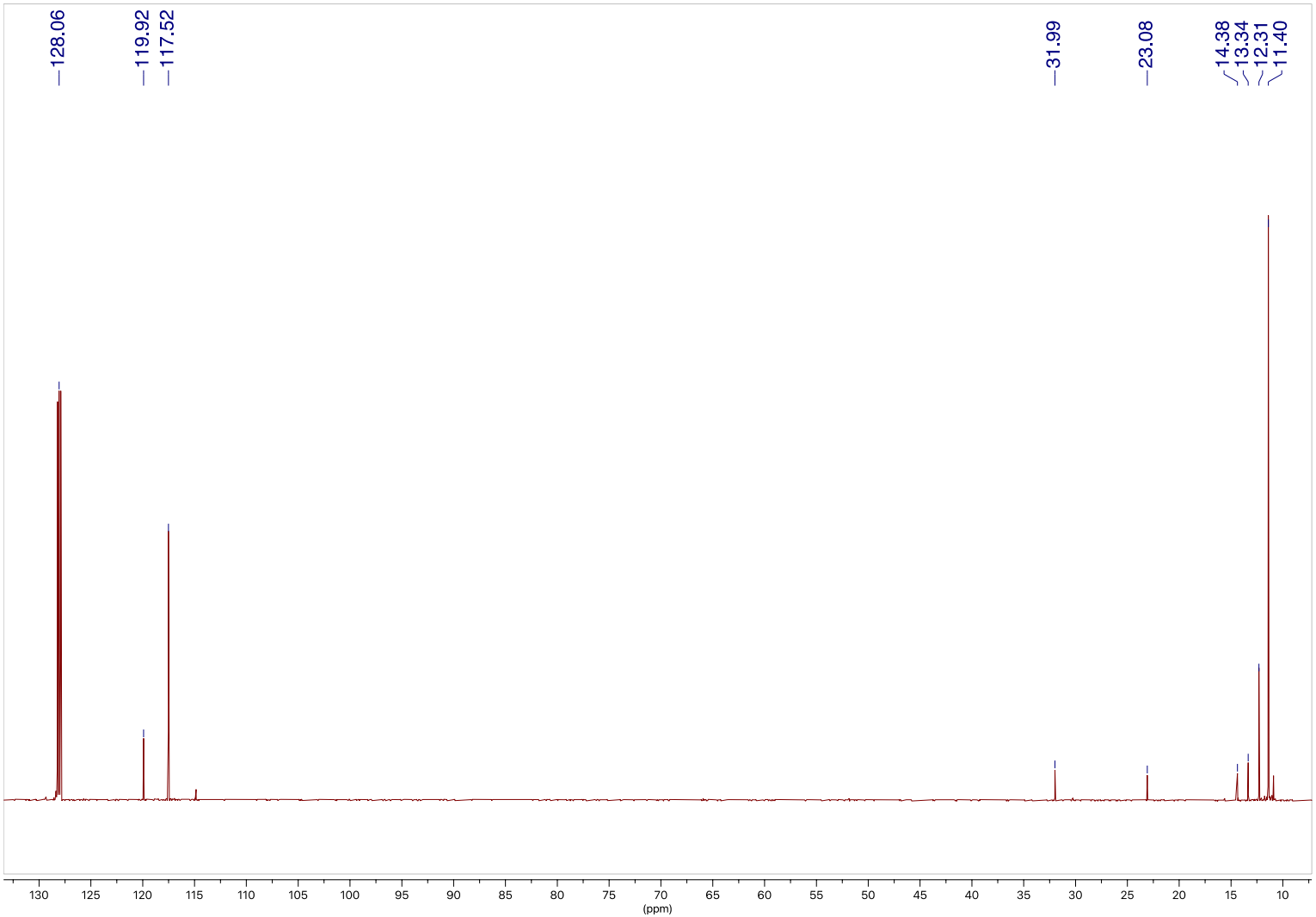

Figure S6. $^{13}C\{^{1}H\}$ NMR spectrum of Cp*Sc[(μ-η^2:η^2-N_2)ScCp*$_2$]$_2$. Signals at 31.99, 23.08, and 14.38 correspond to residual *n*-hexane solvent. 151 MHz, C_6D_6, 298 K.

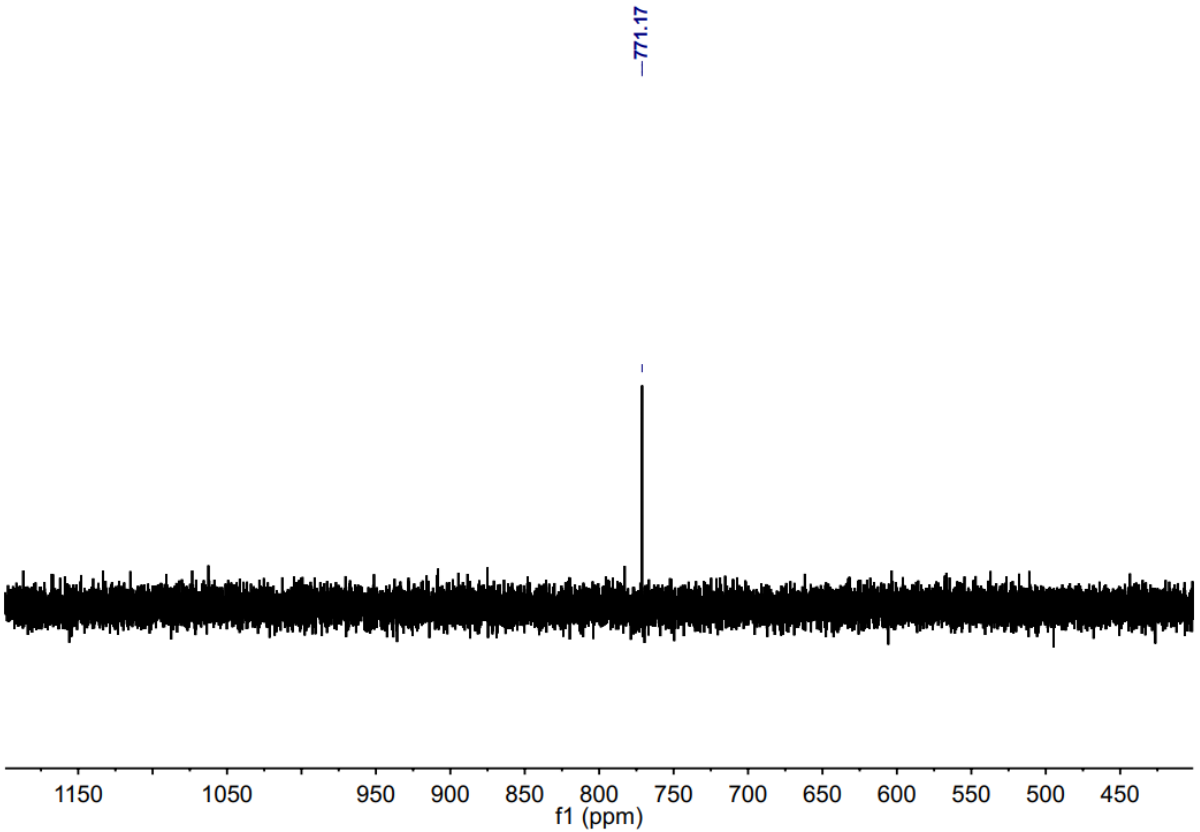

Figure S7. $^{15}N\{^{1}H\}$ NMR spectrum of **^{15}N-2**. 61 MHz, d^8-toluene, 298 K.

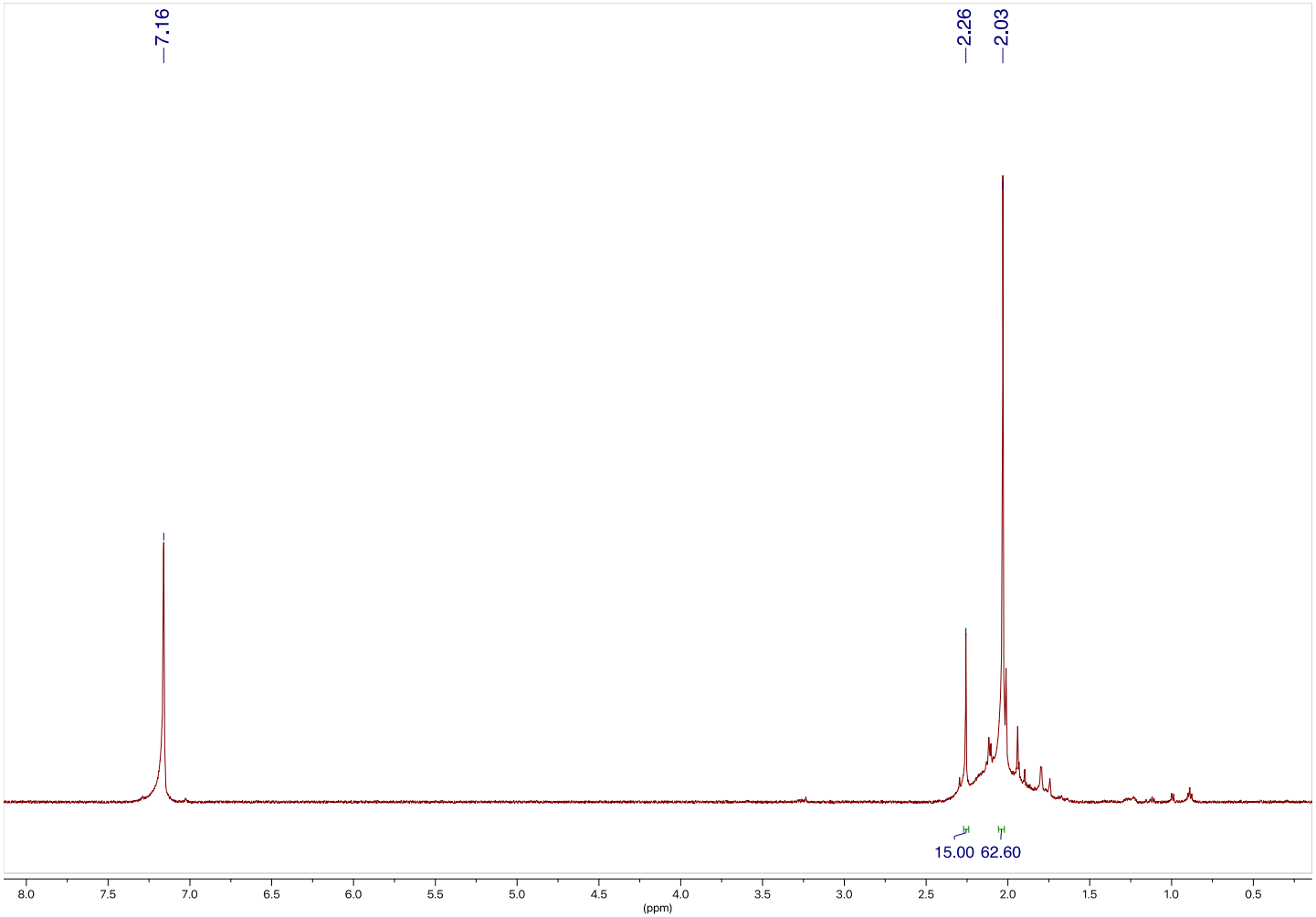

Figure S8. ^{1}H NMR spectrum of the reaction product between Cp*Sc[(μ-η^{2}:η^{2}-N_2)ScCp*$_2$]$_2$ **2**, and N_2O. 600 MHz, C_6D_6, 298 K.

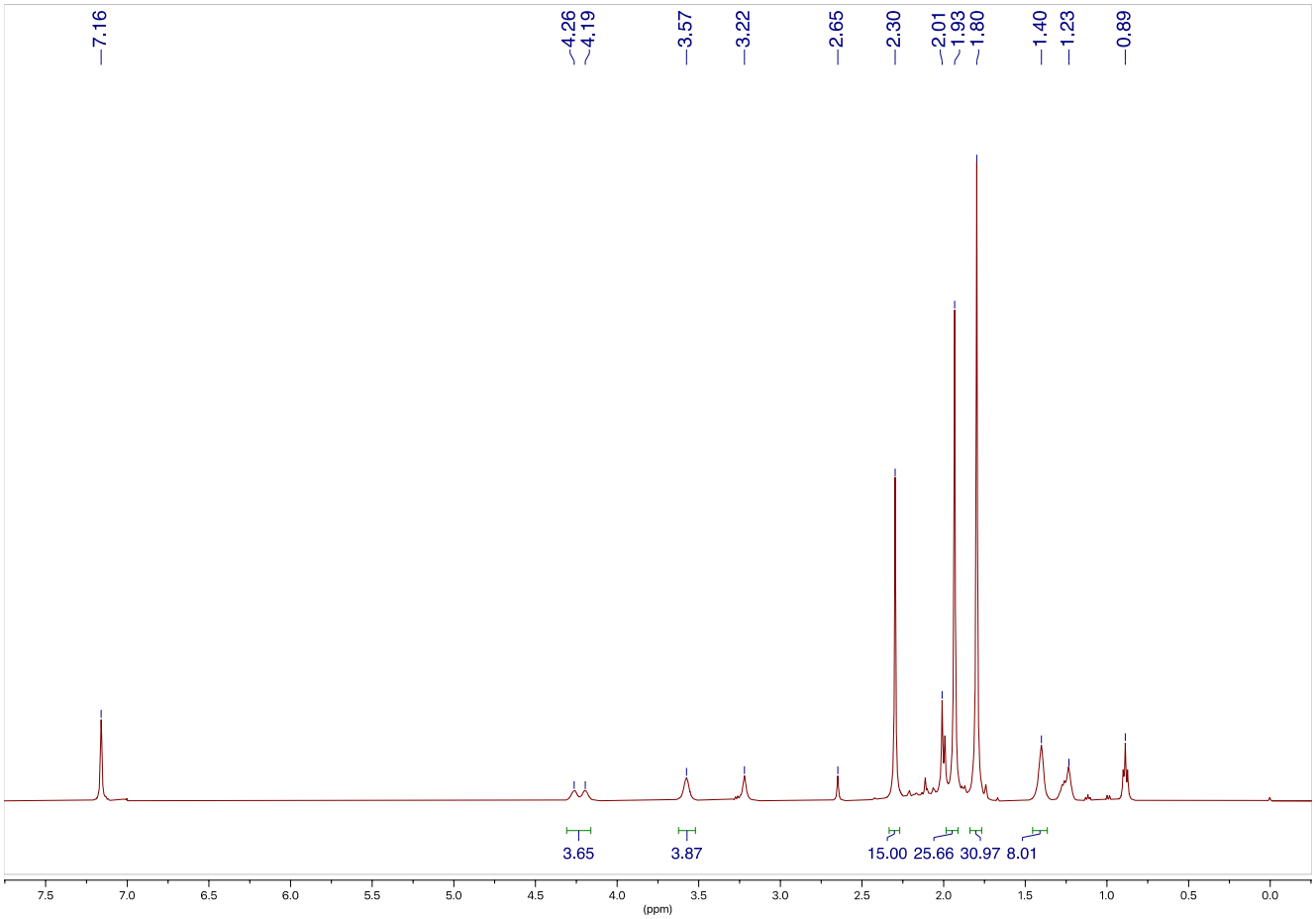

Figure S9. ^{1}H NMR spectrum of crude $Cp^*_2Sc(\mu\text{-}\eta^x\text{:}\eta^x\text{-}N_2)ScI(THF)Cp^*$, **3**. The signal at 1.93 ppm corresponds to a a Cp* containing impurity and the signal at 2.01 ppm is presumably $(Cp^*_2Sc)_2(\mu\text{-}O)$. Signals at 0.89 and 1.23 correspond to n-hexane, the signal at 3.57 ppm corresponds to uncoordinated THF, while those at 3.22 and 2.65 ppm are from unknown species. 500 MHz, C_6D_6, 298 K.

Raman Spectra

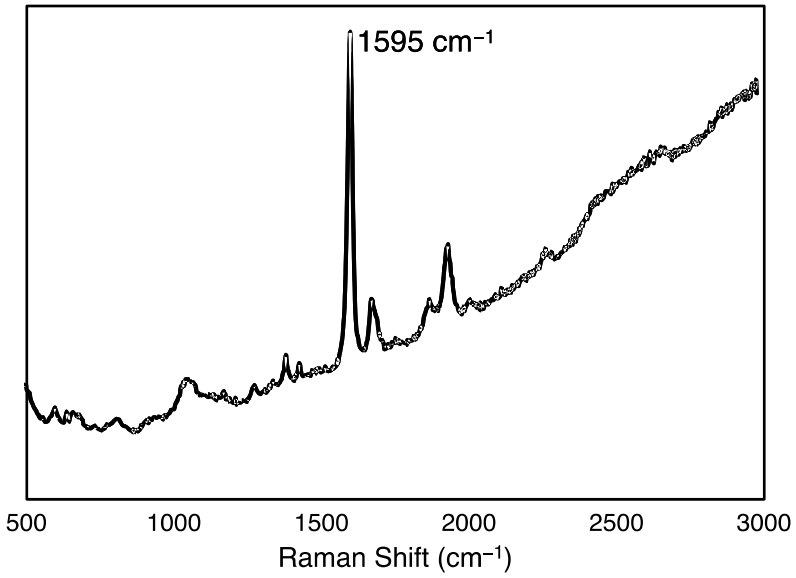

Figure S10. Raman spectrum of **1 (1595 cm^{-1})**.

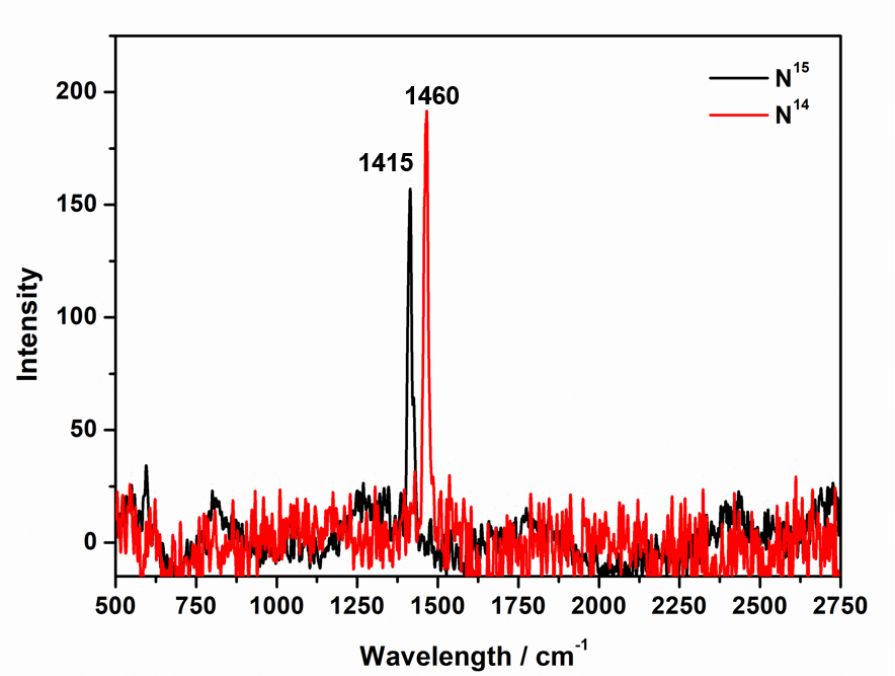

Figure S11 Raman spectra of **2 (1460 cm^{-1})** (red line) and **^{15}N-2 (1415 cm^{-1})** (black line).

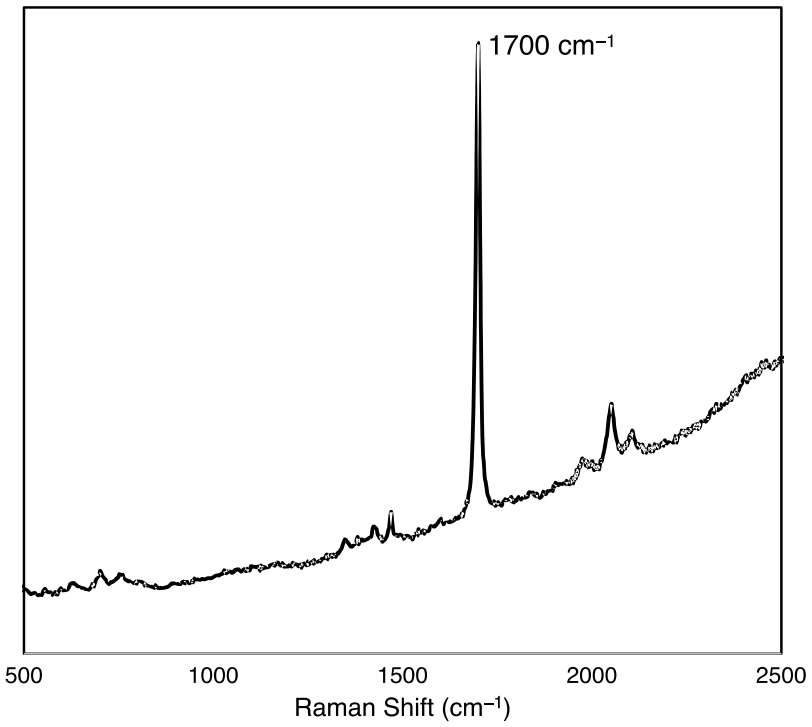

Figure S12. Raman spectru of **3 (1700 cm^{-1})**.

Infrared Spectra

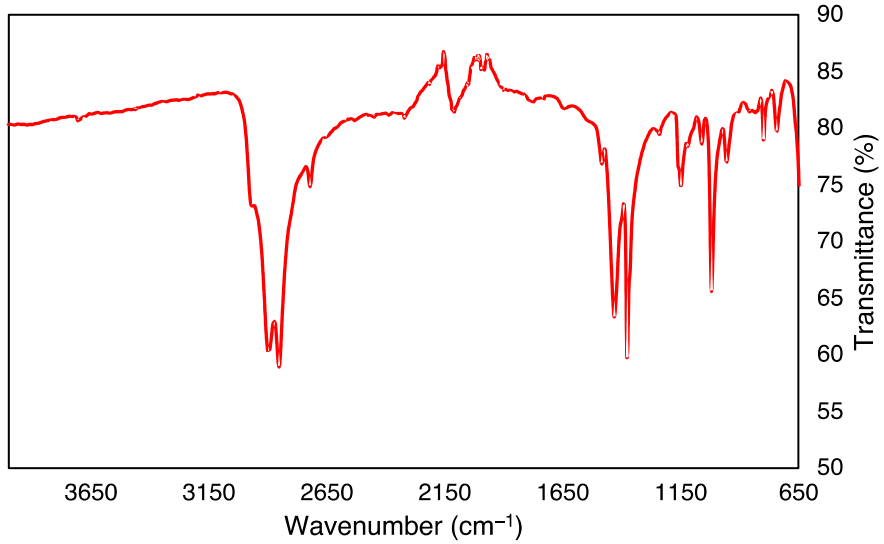

Figure S13. Infrared spectrum of **1**.

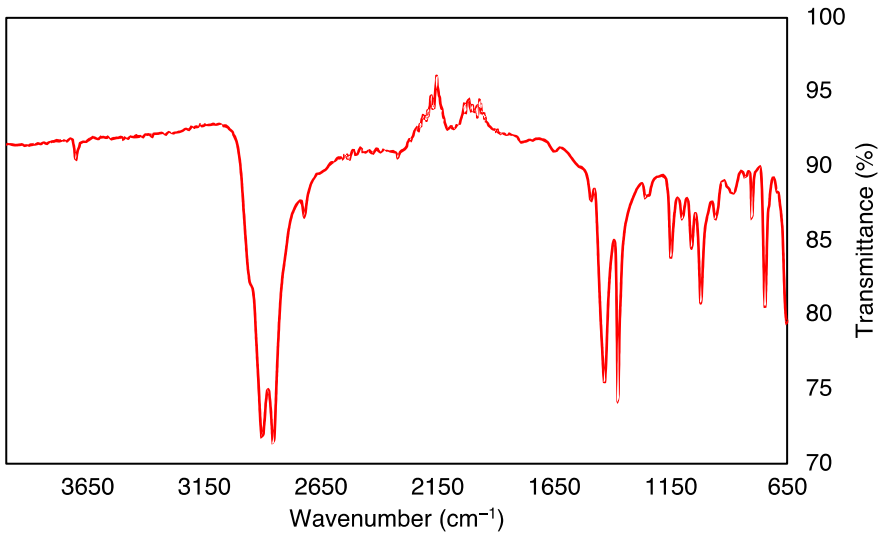

Figure S14. Infrared spectrum of **2**.

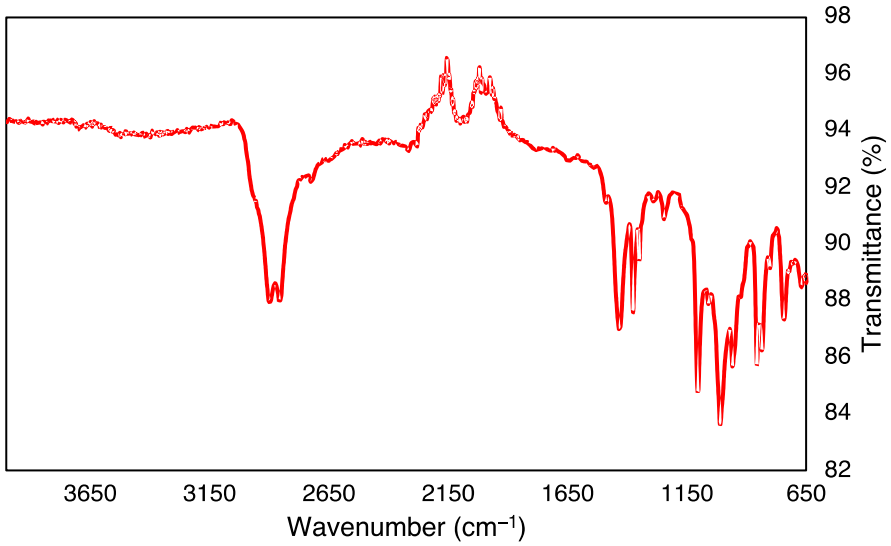

Figure S15. Infrared spectrum of crude **3**.

Computational Details

In this article, we identify the electronic structure, equilibrium geometries, and electronic excitation of the newly synthesized reduced N_2-bridged scandium metallocenes of the formula $Cp^*_2Sc(\mu\text{-}\eta^1\text{:}\eta^1\text{-}N_2)ScCp^*_2$, **1**, $Cp^*Sc[(\mu\text{-}\eta^2\text{:}\eta^2\text{-}N_2)ScCp^*_2]_2$, **2**, and $Cp^*Sc(\mu\text{-}\eta^2\text{:}\eta^2\text{-}N_2)ScI(THF)Cp^*$, **3**, using density functional theory (DFT). Additionally, the hypothesized models of $[(Cp^*)_2Sc]_2(\mu\text{-}\eta^2\text{:}\eta^2\text{-}N_2)$ and $Cp^*_2Sc(\mu\text{-}\eta^1\text{:}\eta^1\text{-}N_2)ScI(THF)Cp^*$ ($Cp^* = C_5Me_5$) are studied for comparison with the end-on and side-on compounds, respectively. Figure S16 shows the optimized structures of **1**-**3** using the methodology described below.

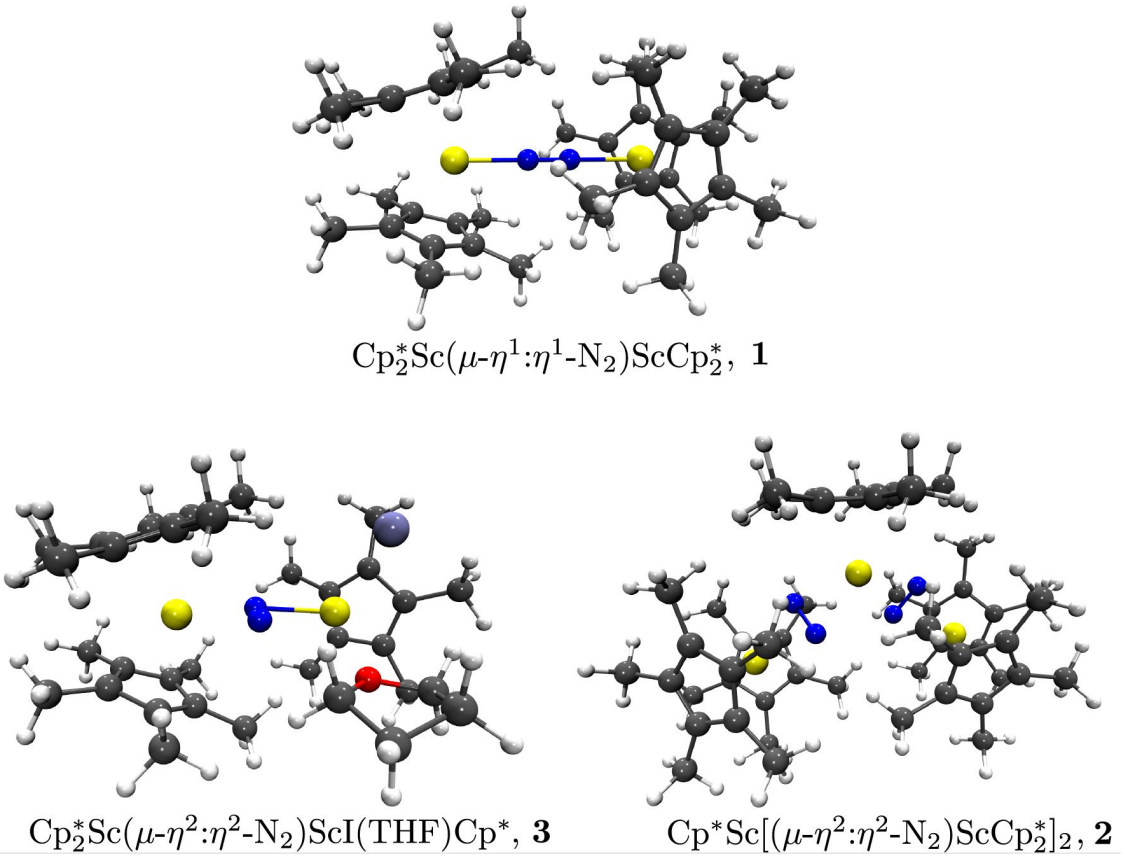

Figure S16. The optimized structures of **1**-**3**.

Methods

The initial structures of **1**-**3** for DFT calculations were obtained from single X-ray diffraction. Starting geometries for side-on $[(Cp^*)_2Sc]_2(\mu\text{-}\eta^2\text{:}\eta^2\text{-}N_2)$ and $Cp^*_2Sc(\mu\text{-}\eta^1\text{:}\eta^1\text{-}N_2)ScI(THF)Cp^*$compounds were constructed from the X-ray structures. All the compounds were optimized using TPSSh density functional[18,19] with Grimme's D3 dispersion correction,[20] including a Becke-Johnson damping function,[21] at the DFT level in the gas phase. Additionally, the resolution of the identity (RI-J) approximation was utilized.[22] Nonmetallic atoms were treated with def2- SV(P)[23] basis sets, while Sc was treated with triple-zeta quality basis sets def2-TZVP.[24,25] The convergence tolerance for geometry and electron density were restricted to 10^{-4}a.u. and 10^{-7}a.u., respectively. Quadrature grids[26] of size 4 were used for numerical integration of the exchange-correlation potential. Harmonic vibrational calculations[27] were performed on the optimized molecular complexes to determine if they correspond to local minima on their potential energy surfaces. Furthermore, triplet instability analysis was performed to test the electronic stability of closed-shell singlets of **2** and **3**. However, no triplet instability was found. For **1**, in order to test if a lower energy open-shell singlet solution exists, the energy of the open-shell singlet was calculated and found to be identical to the closed-shell state as well as its structural parameters.

Additionally, each compound was optimized in the liquid phase using the TPSSh functional and the same basis sets as in the gas phase. The solvation effects of hexane were included by applying the COSMO model[28] with a dielectric constant of 1.887 and an index of refraction of 1.3727. The optimized structures with the COSMO model were verified as local minima through vibrational analysis. The electronic spectra of each optimized compound were simulated using time-dependent density functional theory (TDDFT) calculations employing the non-orthonormal Krylov subspace method.[29] The electronic absorption spectra were calculated using a Gaussian line shape with a width of 0.2 eV centered on the oscillator energy.

The validity of the computational protocol has been thoroughly tested and compared with X-ray structures and UV-Vis of lanthanide molecular complexes, as summarized here.[30] All calculations in this work were performed using the TURBOMOLE quantum chemistry package (version 7.8).[31] The VMD program was used for orbital visualization with a contour value of 0.04.[32]

Results

Electronic structure and Structural parameters

The key structural parameters of **1-3**, from DFT calculations and single X-ray crystals are summarized in the following tables (see Tables S10, S13, S15). Natural population analyses (NPA) for total and spin density are shown below for the ground state of each molecular complex. Kohn-Sham frontier orbitals of Sc compounds are shown in Figure S17. Table S9 presents the compositions of the frontier orbitals as projected by the DFT calculations. The qualitative molecular orbital (MO) diagrams of **1** and **3** are visualized in Figure S18 and Figure S19, respectively.

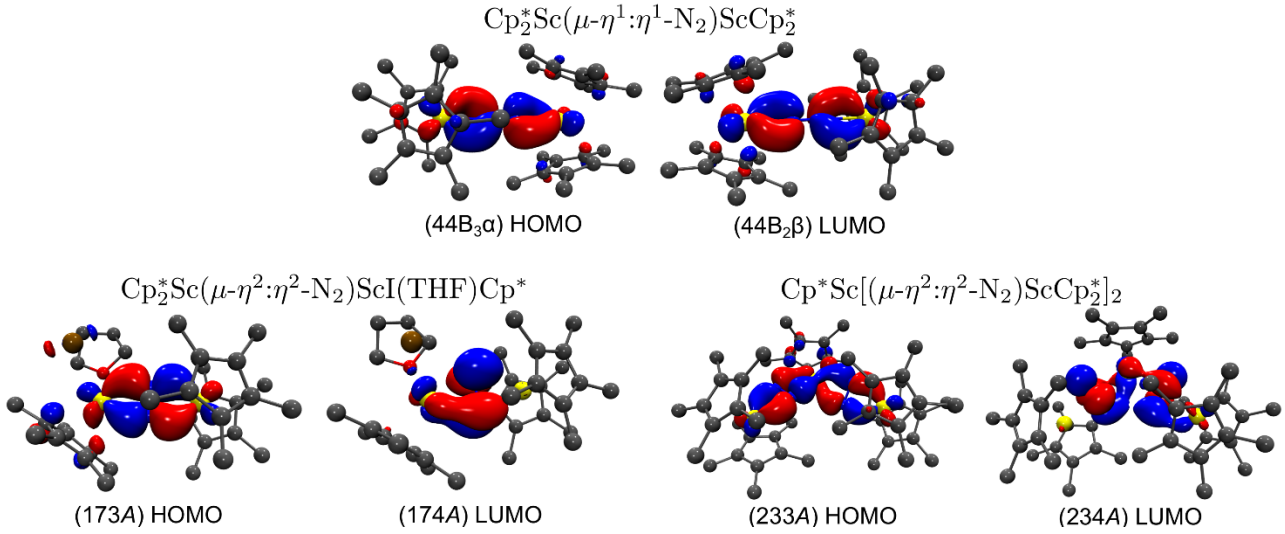

Figure S17. The HOMO and LUMO of each scandium molecular complex are shown, with hydrogen atoms omitted for clarity. A contour value of 0.04 was used to depict the orbitals.

Table S9. Composition of frontier molecular orbitals of Sc molecular structures from Mulliken population analysis (MPA).

Molecular complex	MO	%s	%p	%d	%L
1	(44$B_2\beta$) LUMO	0	2.8	43.42	53.37
	(44$B_3\alpha$) HOMO	0	2.96	35.1	61.3
2	(234A) LUMO	0	0	23.44	75.59
	(233A) HOMO	0	2.64	26.71	69.40
3	(174A) LUMO	0	0	17.58	81.69
	(173A) HOMO	0	2.3	29.88	66.80

Table S10. Relative Energies (eV), Spin States, and Selected Structural Parameters (Calculated and Experimental) of $Cp^*_2Sc(\mu\text{-}\eta^1\text{:}\eta^1\text{-}N_2)ScCp^*_2$: Bond Distances (in Å) and Angles (in °) from DFT and X-ray.

State	^1A	$^3B_1$	X-ray
Rel. Energy(eV)	0.26	0.00	——
Cnt1-Sc(1)-Cnt2	144.5	144.5	146.58
Cnt1-Sc(2)-Cnt2	144.5	144.5	146.58
Sc(1)-Sc(2)	5.298	5.306	5.268
Sc(1)-Cnt	2.150	2.161	2.172
Sc(2)-Cnt	2.150	2.161	2.172
Sc(1)-N(1)	2.059	2.060	2.045
Sc(2)-N(1′)	2.059	2.060	2.045
N(1)-N(1′)	1.181	1.187	1.177
Sc(1)- N(1)-N(1′)	179.0	180.0	180.0
Sc(2)- N(1)-N(1′)	179.0	180.0	180.0

Table S11. Atomic populations analysis from NPA (total density) for triplet (S=1) $Cp^*_2Sc(\mu\text{-}\eta^1\text{:}\eta^1\text{-}N_2)ScCp^*_2$

Atom	Charge	n(s)	n(p)	n(d)
Sc(1)	1.843	6.083	12.006	1.064
Sc(2)	1.843	6.083	12.006	1.064
N(1′)	-0.471	3.495	3.970	0.006
N(1)	-0.471	3.495	3.970	0.006

Table S12. Atomic populations analysis from NPA (spin density) for triplet (S=1) $Cp^*_2Sc(\mu\text{-}\eta^1\text{:}\eta^1\text{-}N_2)ScCp^*_2$

Atom	Sum	n(s)	n(p)	n(d)
Sc(1)	0.446	0.002	0.040	0.398
Sc(2)	0.446	0.002	0.040	0.398
N(1′)	0.453	0.101	0.442	0.000
N(1)	0.453	0.101	0.442	0.000

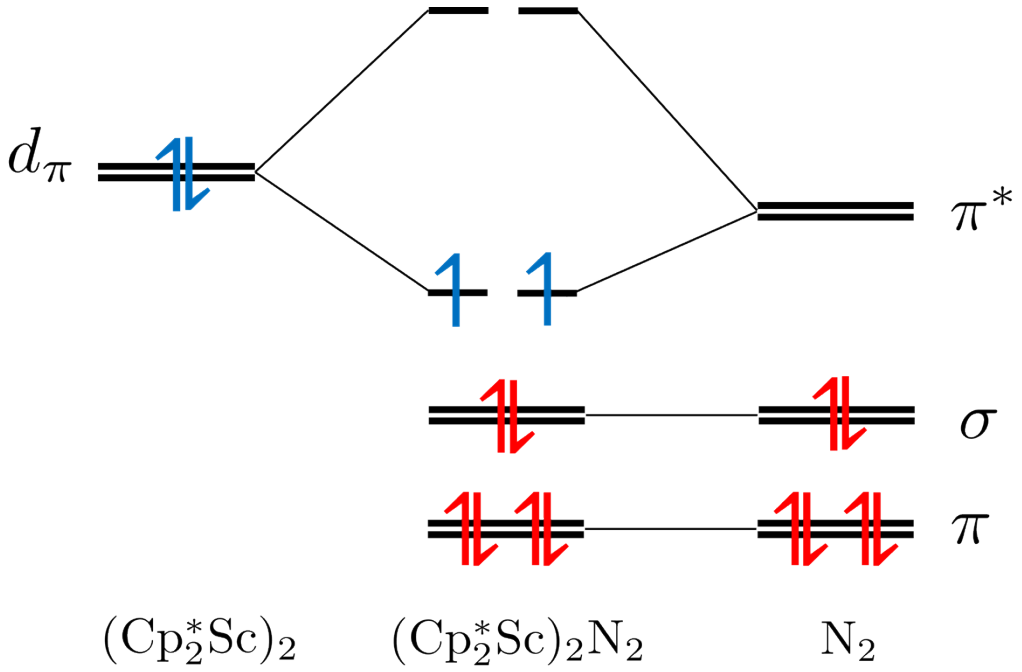

Figure S18. Qualitative MO diagram of triplet (S=1) $Cp^*_2Sc(\mu\text{-}\eta^1\text{:}\eta^1\text{-}N_2)ScCp^*_2$

Table S13. Relative Energies (eV), Spin States, and Selected Structural Parameters (Calculated and Experimental) of $Cp^*Sc[(\mu\text{-}\eta^2\text{:}\eta^2\text{-}N_2)ScCp^*_2]_2$: Bond Distances (in Å) and Angles (in °)

State	^1A	^3A	^5A	X-ray
Rel. Energy(eV)	0	0.97	2.22	——
Cnt1-Sc(1)-Cnt2	140.9	141.1	139.1	140.1
Cnt3-Sc(3)-Cnt4	143.2	142.1	141.7	141.5
Sc(1)-Sc(2)	4.204	4.211	4.168	4.161
Sc(2)-Sc(3)	4.060	4.109	4.084	4.109
Sc(1)-Cnt(ave)	2.178	2.173	2.180	2.193
Sc(2)-Cnt	2.174	2.144	2.143	2.167
Sc(3)-Cnt(ave)	2.180	2.177	2.169	2.184
Sc(1)-N(1)(ave)	2.187	2.229	2.249	2.169
Sc(2)-N(1′)(ave)	2.184	2.181	2.246	2.173
Sc(3)-N(1′)(ave)	2.159	2.177	2.244	2.159
N(1)-N(1′)	1.266	1.241	1.245	1.228
N(2)-N(2′)	1.240	1.244	1.252	1.231

Table S14. Atomic populations analysis from NPA (total density) for singlet (S=0) $Cp^*Sc[(\mu\text{-}\eta^2\text{:}\eta^2\text{-}N_2)ScCp^*_2]_2$

Atom	Charge	n(s)	n(p)	n(d)
Sc(1)	1.800	6.102	12.007	1.088
Sc(2)	1.738	6.120	12.009	1.129
Sc(3)	1.833	6.100	12.006	1.058
N(1′)	-0.521	3.555	3.961	0.009
N(1)	-0.524	3.555	3.960	0.009
N(2′)	-0.589	3.566	4.014	0.009
N(2)	-0.556	3.562	3.985	0.009

Table S15. Relative Energies (eV), Spin States, and Selected Structural Parameters (Calculated and Experimental) of $Cp^*_2Sc(\mu\text{-}\eta^2\text{:}\eta^2\text{-}N_2)ScI(THF)Cp^*$: Bond Distances (in Å) and Angles (in °)

State	^1A	^3A	X-ray
Rel. Energy(eV)	0	+1.16	——
Cnt1-Sc(1)-Cnt2	142.7	142.0	141.5
Sc(1)-Sc(2)	4.134	4.440	4.218
Sc(1)-Cnt(ave)	2.170	2.163	2.185
Sc(2)-Cnt	2.171	2.159	2.198
Sc(1)-N(1)	2.171	2.142	2.217
Sc(2)-N(1′)	2.145	2.057	2.172
N(1)-N(1′)	1.236	1.217	1.217
Sc(2)-I	2.847	2.818	2.863
Sc(2)-O	2.228	2.207	2.216

Table S16. Atomic populations analysis from NPA (total density) for singlet (S=0) $Cp^*_2Sc(\mu\text{-}\eta^2\text{:}\eta^2\text{-}N_2)ScI(THF)Cp^*$

Atom	Charge	n(s)	n(p)	n(d)
Sc(1)	1.733	6.106	12.006	1.151
Sc(2)	1.515	6.184	12.009	1.288
N(1′)	-0.532	3.556	3.966	0.009
N(1)	-0.549	3.555	3.985	0.009

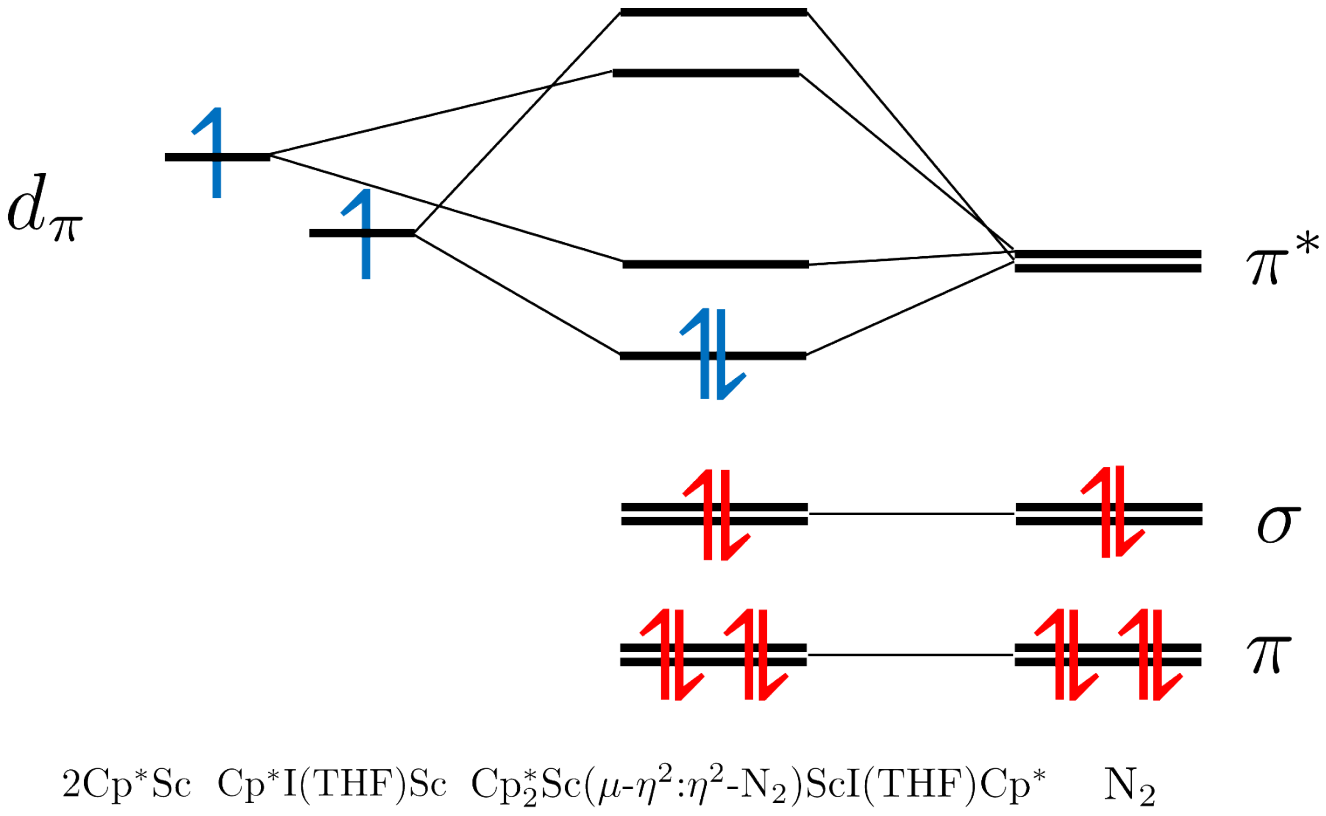

Figure S19. Qualitative MO diagram of singlet (S=0) $Cp^*_2Sc(\mu\text{-}\eta^2\text{:}\eta^2\text{-}N_2)ScI(THF)Cp^*$.

Absorption Spectra

The electronic spectra simulated using TDDFT calculations are displayed below for each metal complex. The main transitions are tabulated below.

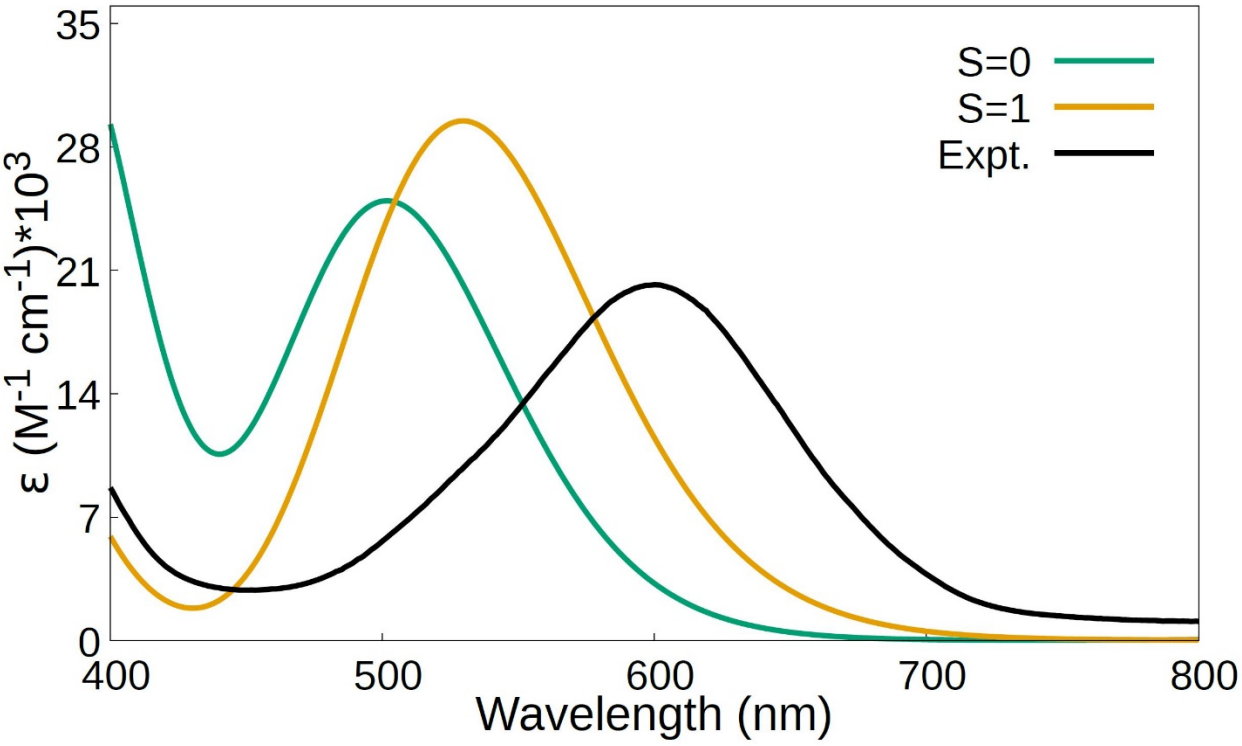

Figure S20.: Simulated and experimental UV-Vis spectra of $Cp^*_2Sc(\mu\text{-}\eta^1\text{:}\eta^1\text{-}N_2)ScCp^*_2$. A Gaussian spectral lineshape with a width of 0.2 eV was employed.

Table S17. Electronic excitation summary for $Cp^*_2Sc(\mu\text{-}\eta^1\text{:}\eta^1\text{-}N_2)ScCp^*_2$. All excitations computed are single excitations involving alpha spin to alpha spin transitions. Oscillator strengths are reported in the length gauge. Only the dominant contributions to the overall excitation are reported.

Wavelength (nm)	Osc. Str.	Dominant contributions			
		Occupied(eV)	Virtual(eV)	% weight	Exc. type
530	0.515	$44B_2\alpha$(-3.11)	$45B_3\alpha$(-0.48)	51.1	L(p)/M(d)→M(d)
		$44B_3\alpha$(-2.99)	$45B_2\alpha$(-0.37)	43.2	L(p)/M(d)→M(d)
364	0.138	$43B_2\beta$(-5.13)	$44B_3\beta$(-1.34)	71.9	L→M(d)/L(p)

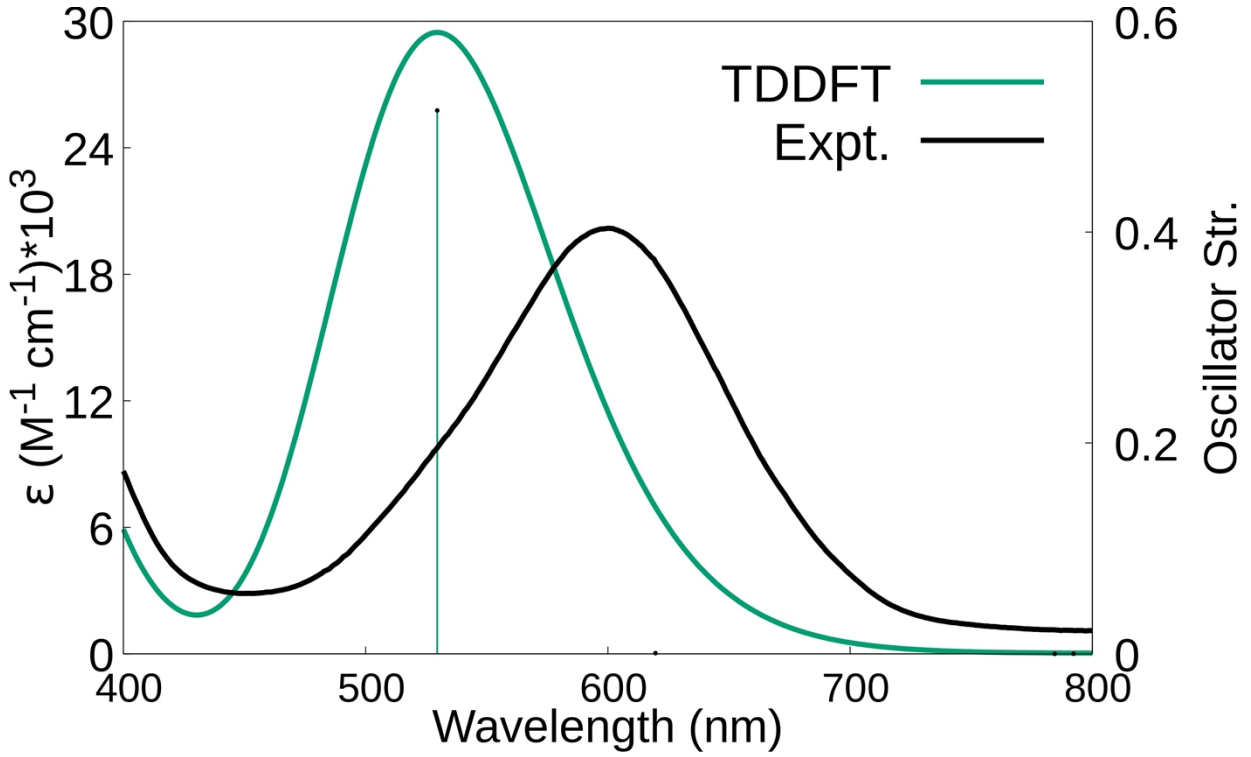

Figure S21. Simulated and experimental UV-Vis spectra of triplet (S=1) $Cp^*_2Sc(\mu\text{-}\eta^1\text{:}\eta^1\text{-}N_2)ScCp^*_2$. A Gaussian spectral lineshape with a width of 0.2 eV was employed.

Table S18. Molecular orbital energies and Mulliken population analysis (MPA) of triplet (S=1) $Cp^*_2Sc(\mu\text{-}\eta^1\text{:}\eta^1\text{-}N_2)ScCp^*_2$ complex. The % metal character identifies the overall metal contribution from both Sc centers combined to the molecular orbital, the %d character identifies how much of the total orbital originates directly from the metal d orbitals. The % L character shows the overall contribution of the two nitrogens of the bridged N_2.

Orbital		Energy(eV)	% Metal	% d	% L
LUMO+13	$46B_2\alpha$	1.15	28.4	18.1	0
LUMO+18	$46B_3\alpha$	1.04	32.1	22.8	0
LUMO+7	$45B_2\alpha$	-0.37	46.3	44.5	25.2
LUMO+6	$45B_3\alpha$	-0.48	47.2	45.8	24.0
LUMO+1	$44B_3\beta$	-1.34	51.3	48.3	38.5
LUMO	$44B_2\beta$	-1.50	46.6	43.4	35.5
HOMO	$44B_3\alpha$	-2.99	38.7	35.1	48.7
HOMO-1	$44B_2\alpha$	-3.11	40.1	40.1	46.9
HOMO-2	$43B_2\beta$	-5.13	10.7	7.7	0
HOMO-3	$43B_3\beta$	-5.14	7.5	2.6	0

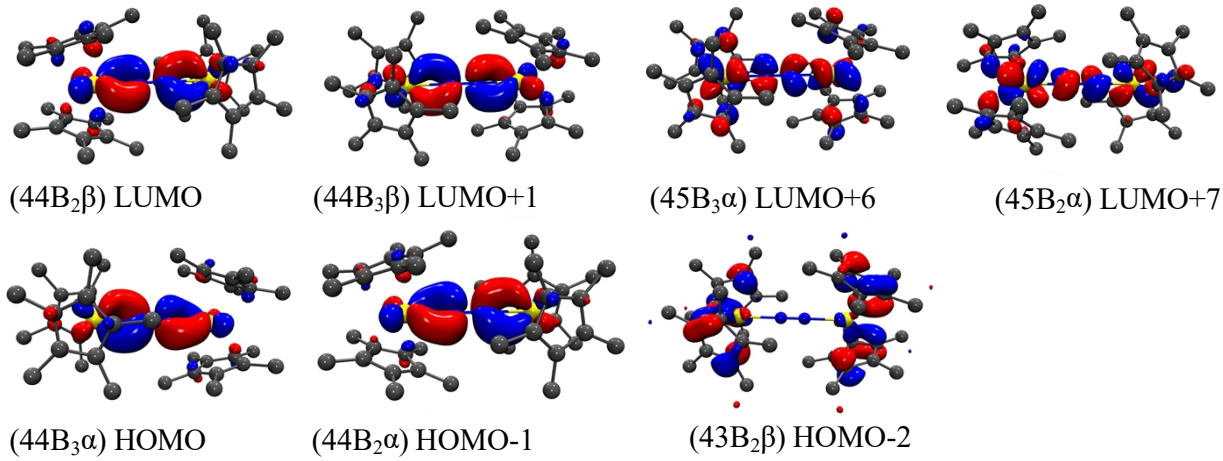

Figure S22. Molecular orbital plots of triplet (S=1) $Cp^*_2Sc(\mu\text{-}\eta^1\text{:}\eta^1\text{-}N_2)ScCp^*_2$ complex are shown, with hydrogen atoms omitted for clarity. A contour value of 0.04 was used to depict the orbitals.

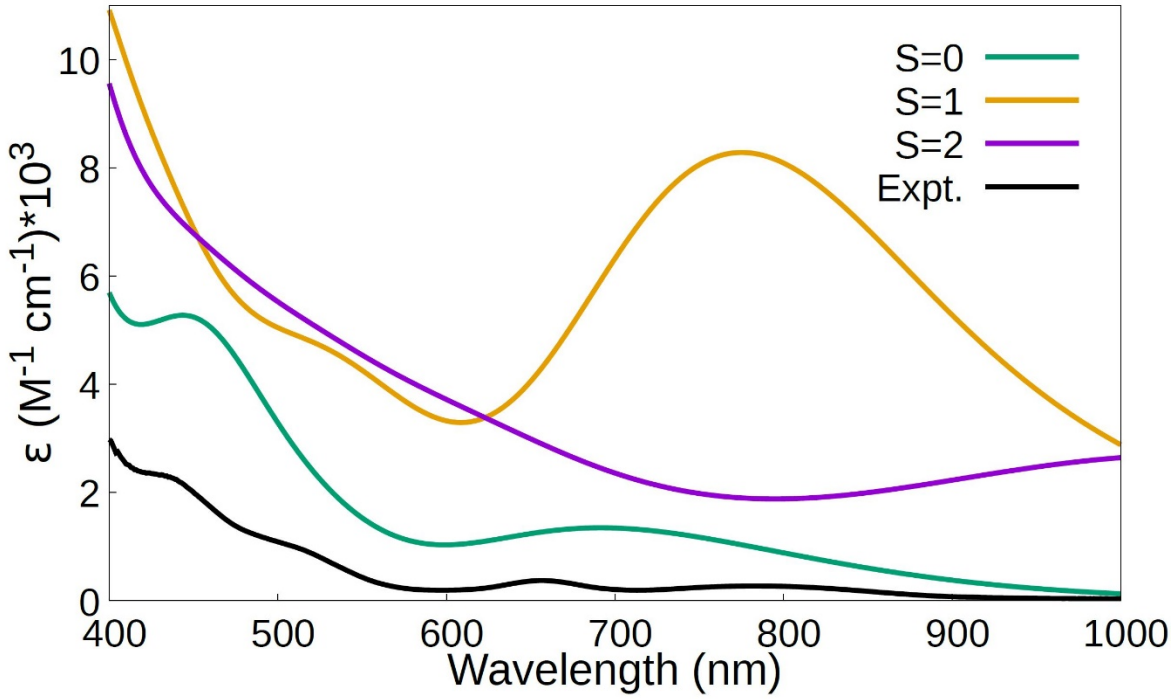

Figure S23. Simulated UV-Vis spectra of $Cp^*Sc[(\mu\text{-}\eta^2\text{:}\eta^2\text{-}N_2)ScCp^*_2]_2$. A Gaussian spectral lineshape with a width of 0.2 eV was employed.

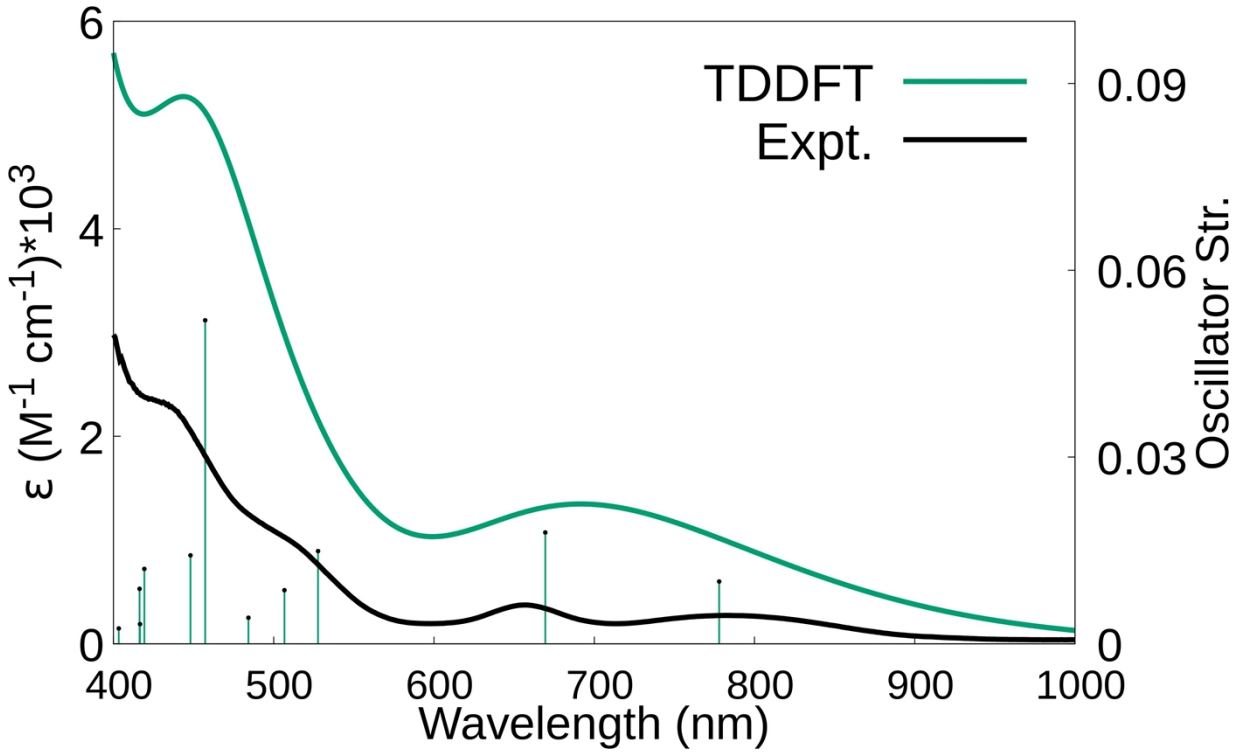

Figure S24. Simulated and experimental UV-Vis spectra of singlet(S=0) $Cp^*Sc[(\mu\text{-}\eta^2\text{:}\eta^2\text{-}N_2)ScCp^*_2]_2$. A Gaussian spectral lineshape with a width of 0.2 eV was employed.

Table S19. Molecular orbital energies and Mulliken population analysis (MPA) of $Cp^*Sc[(\mu\text{-}\eta^2\text{:}\eta^2N_2)ScCp^*_2]_2$ singlet complex. The % metal character identifies the overall metal contribution from both Sc centers combined to the molecular orbital, the %d character identifies how much of the total orbital originates directly from the metal d orbitals. The % L character shows the overall contribution of the four nitrogens of the two bridged N_2.

Orbital		Energy(eV)	% Metal	% d	% L
LUMO+14	248*A*	+1.056	69.00	65.90	1.57
LUMO+7	241*A*	+0.087	69.00	65.90	4.81
LUMO+6	240*A*	-0.081	56.40	55.05	9.71
LUMO+5	239*A*	-0.461	65.30	55.23	22.05
LUMO+4	238*A*	-0.648	71.00	67.76	12.43
LUMO+1	235*A*	-1.461	30.35	26.30	65.75
LUMO	234*A*	-1.758	24.41	23.44	72.95
HOMO	233*A*	-3.897	36.00	26.71	54.71
HOMO-1	232*A*	-4.657	37.36	34.42	57.81
HOMO-6	227*A*	-5.300	12.79	11.00	3.77
HOMO-9	224*A*	-5.438	15.03	13.44	0.00

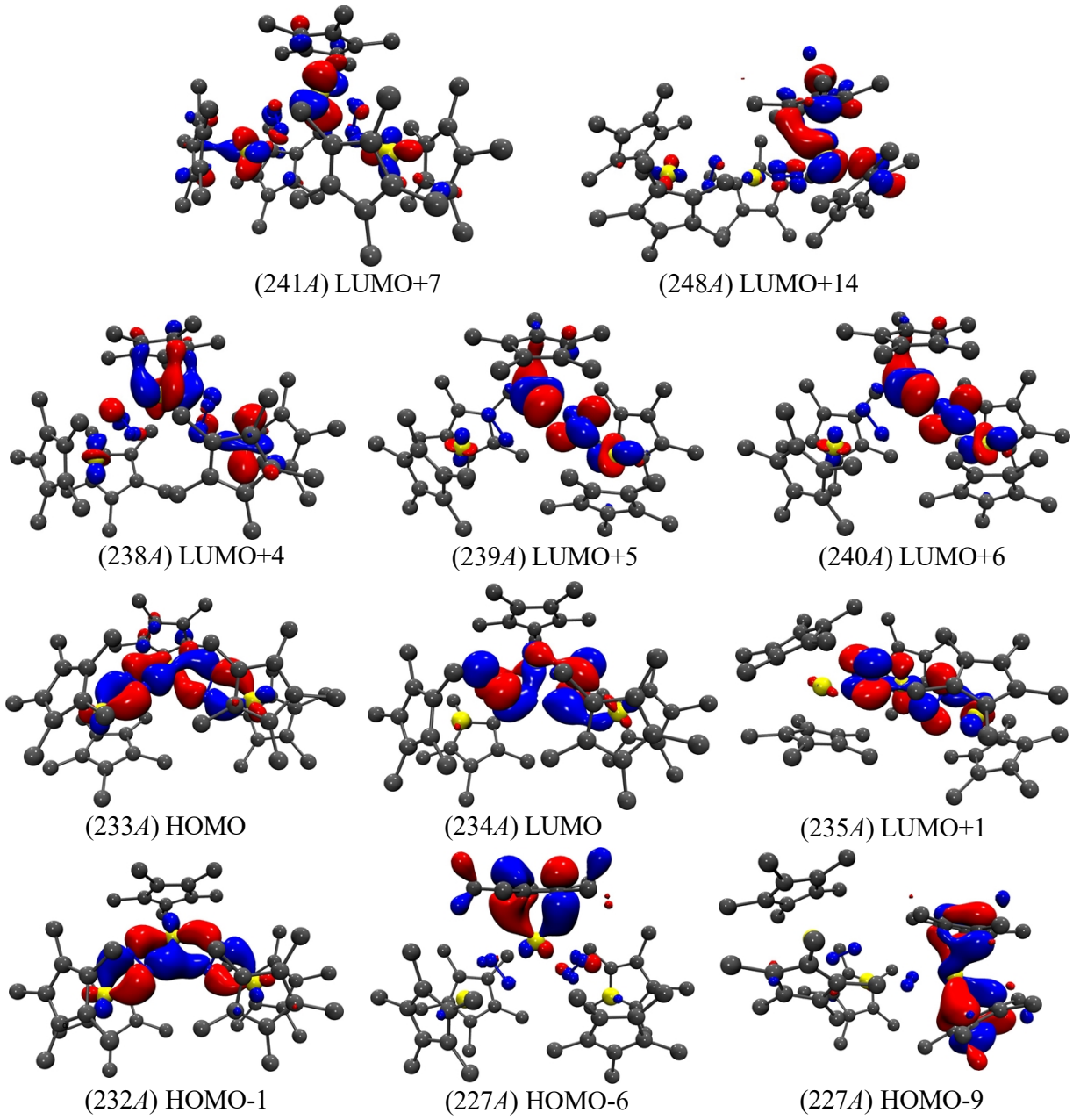

Figure S25. Molecular orbital plots of singlet(S=0) $Cp^*Sc[(\mu\text{-}\eta^2\text{:}\eta^2\text{-}N_2)ScCp^*_2]_2$ complex are shown, with hydrogen atoms omitted for clarity. A contour value of 0.04 was used to depict the orbitals.

Table S20. Electronic excitation summary for $Cp^*Sc[(\mu\text{-}\eta^2\text{:}\eta^2\text{-}N_2)ScCp^*_2]_2$. All excitations computed are single excitations involving alpha spin to alpha spin transitions. Oscillator strengths are reported in the length gauge. Only the dominant contributions to the overall excitation are reported.

Wavelength (nm)	Osc. Str.	Dominant contributions			
		Occupied(eV)	Virtual(eV)	% weight	Exc. type
778	0.010	233*A*(-3.90)	234*A*(-1.76)	92.9	L(p)/M(d)→L(p)
669	0.018	233*A*(-3.90)	235*A*(-1.46)	82.9	L(p)/M(d)→L(p)
528	0.015	232*A*(-4.66)	234*A*(-1.76)	49.5	L(p)/M(d)→L(p)
		233*A*(-3.90)	235*A*(-1.46)	33.8	L(p)/M(d)→L(p)
457	0.052	232*A*(-4.66)	235*A*(-1.46)	63.0	L(p)/M(d)→L(p)
347	0.132	233*A*(-3.90)	240*A*(-0.08)	41.9	L(p)/M(d)→M(d)
		233*A*(-3.90)	241*A*(0.09)	21.5	L(p)/M(d)→M(d)
274	0.125	232*A*(-4.66)	240*A*(-0.08)	20.1	L(p)/M(d)→M(d)
		224*A*(-5.44)	238*A*(-0.65)	10.6	L(p)→M(d)
		227*A*(-5.30)	239*A*(-0.46)	10.2	L(p)→M(d)
		233*A*(-3.90)	248*A*(1.06)	9.6	L(p)/M(d)→M(d)

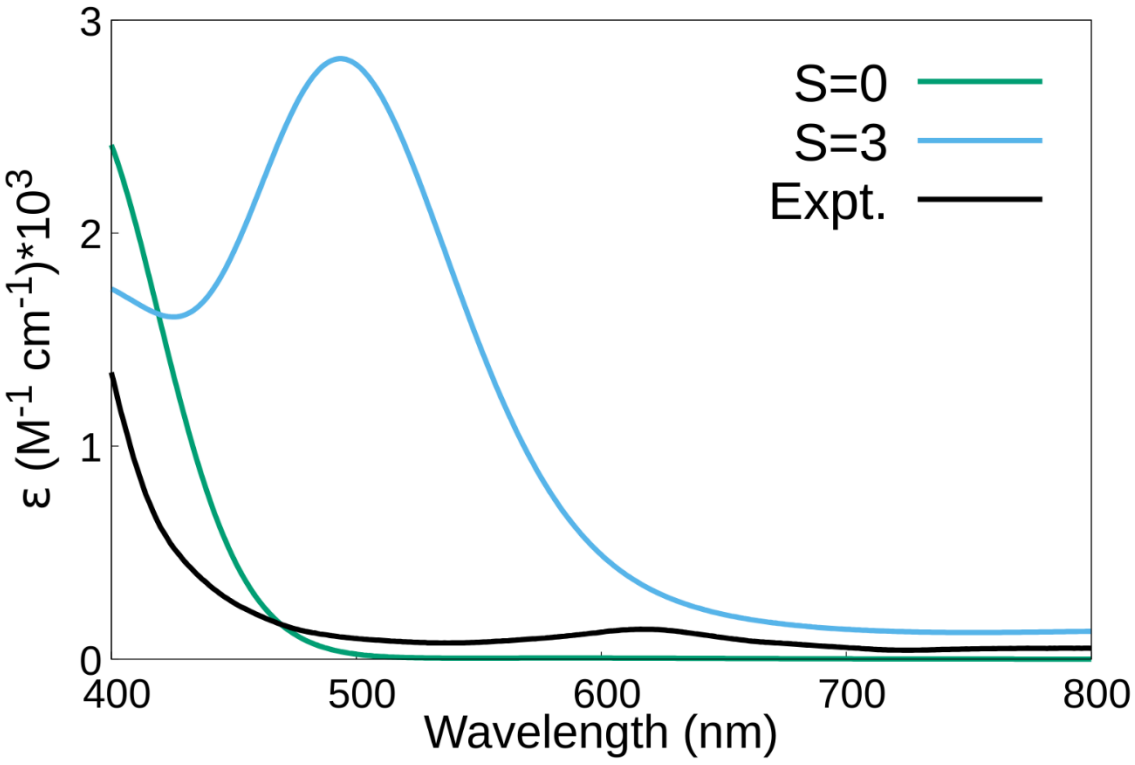

Figure S26. Simulated UV-Vis spectra of $Cp^*_2Sc(\mu\text{-}\eta^2\text{:}\eta^2\text{-}N_2)ScI(THF)Cp^*$. A Gaussian spectral lineshape with a width of 0.2 eV was employed. The calculated absorption spectrum of the triplet state (S=1) was scaled by a factor of 0.25

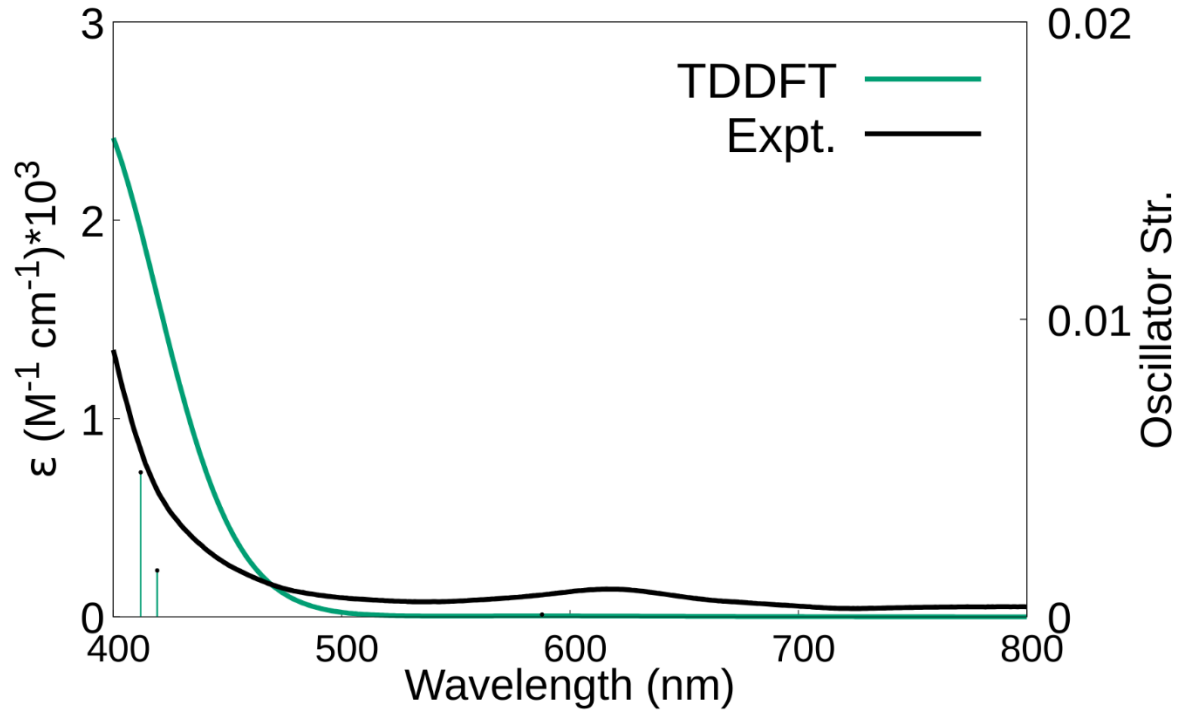

Figure S27. Simulated UV-Vis spectra of singlet (S=0) $Cp^*_2Sc(\mu\text{-}\eta^2\text{:}\eta^2\text{-}N_2)ScI(THF)Cp^*$. A Gaussian spectral lineshape with a width of 0.2 eV was employed.

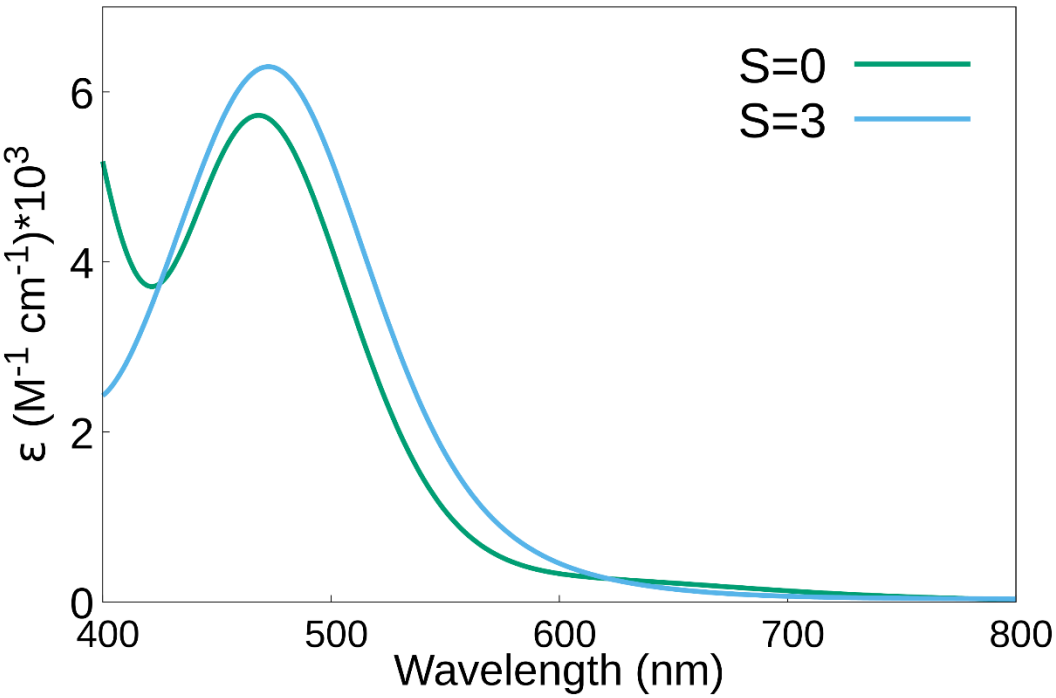

Figure S28. Simulated UV-Vis spectra of $Cp^*_2Sc(\mu\text{-}\eta^1\text{:}\eta^1\text{-}N_2)ScI(THF)Cp^*$. A Gaussian spectral lineshape with a width of 0.2 eV was employed. The calculated absorption spectra were scaled by a factor of 0.25.

Table S21. Electronic excitation summary for singlet (S=0) $Cp^*_2Sc(\mu\text{-}\eta^2\text{:}\eta^2\text{-}N_2)ScI(THF)Cp^*$. All excitations computed are single excitations involving alpha spin to alpha spin transitions. Oscillator strengths are reported in the length gauge. Only the dominant contributions to the overall excitation are reported.

Wavelength (nm)	Osc. Str.	Dominant contributions			
		Occupied(eV)	Virtual(eV)	% weight	Exc. type
588	0.0001	173*A(*-4.65)	174*A(*-1.77)	97.2	M(d)→L(p)
412	0.005	173*A(*-4.65)	175*A(*-1.05)	87.6	M(d)→M(d)
360	0.017	167*A(*-5.56)	174*A(*-1.77)	96.2	L(p)/M(d)→L(p)
304	0.063	172*A(*-5.13)	177*A(*-0.70)	43.2	L(p)/M(d)→M(d)
		173*A(*-4.65)	178*A(*-34.8)	34.8	M(d)→M(d)
296	0.206	172*A(*-5.13)	177*A(*-0.70)	35.7	L(p)/M(d)→M(d)
		173*A(*-4.65)	178*A(*-0.39)	20.7	M(d)→M(d)
203	0.110	173*A(*-4.65)	194*A(*1.81)	35.5	M(d)→M(d)
		168*A(*-5.49)	183*A(*0.89)	12.8	L(p)→M(d)
		171*A(*-5.22)	184*A(*0.96)	8.1	L(p)→M(d)

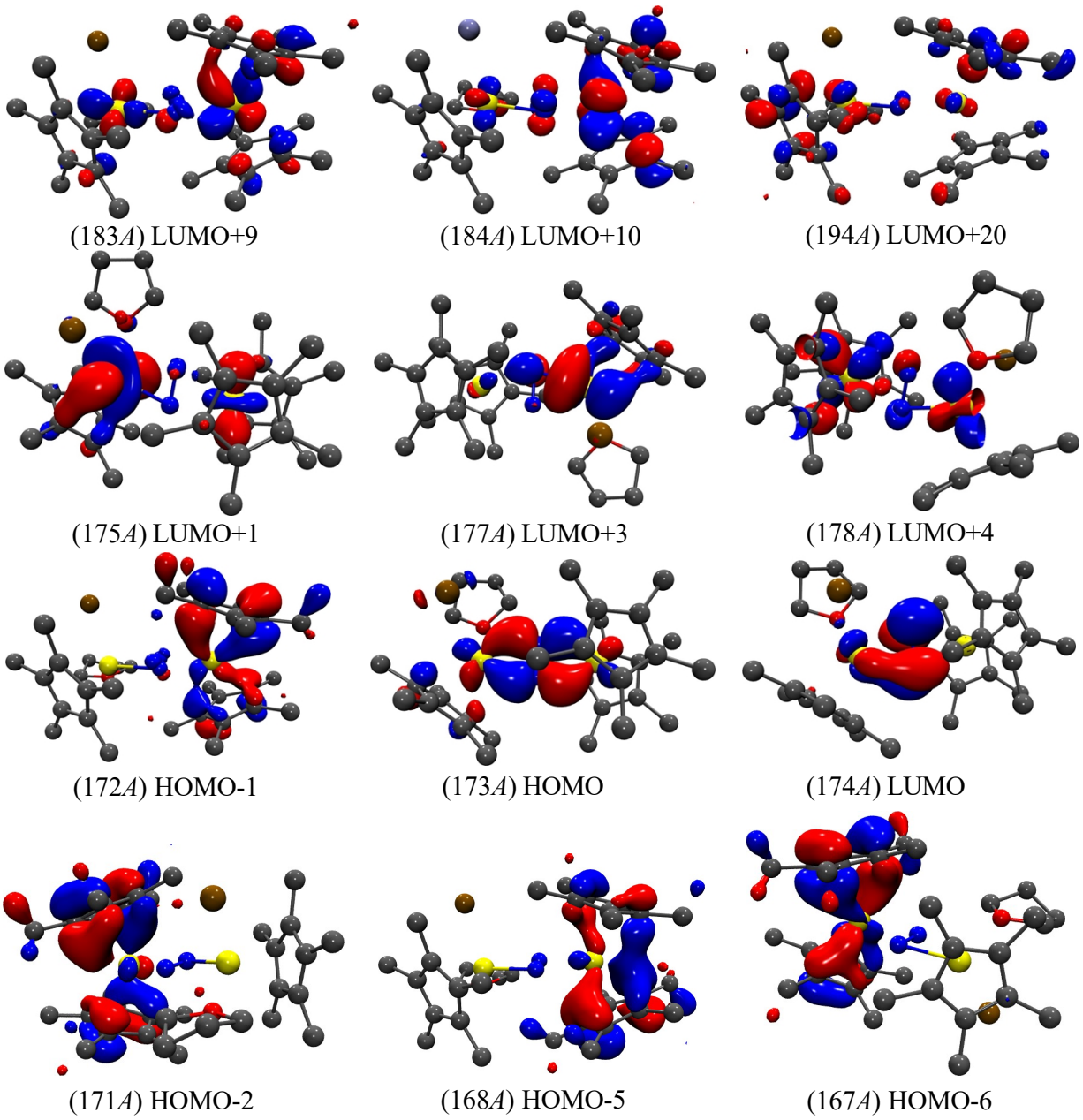

Figure S29. Molecular orbital plots of singlet (S=0) $Cp^*_2Sc(\mu\text{-}\eta^2\text{:}\eta^2\text{-}N_2)ScI(THF)Cp^*$ complex are shown, with hydrogen atoms omitted for clarity. A contour value of 0.04 was used to depict the orbitals.

Table S22. Molecular orbital energies and Mulliken population analysis (MPA) of $Cp^*_2Sc(\mu\text{-}\eta^2\text{:}\eta^2\text{-}N_2)ScI(THF)Cp^*$ singlet complex. The % metal character identifies the overall metal contribution from both Sc centers combined to the molecular orbital, the %d character identifies how much of the total orbital originates directly from the metal d orbitals. The % L character shows the overall contribution of the two nitrogens of the bridged N_2.

Orbital		Energy(eV)	% Metal	% d	% L
LUMO+20	194*A*	+1.810	19.25	15.12	0.00
LUMO+10	184*A*	+0.959	52.71	51.64	7.09
LUMO+9	183*A*	+0.893	67.12	57.57	2.75
LUMO+4	178*A*	-0.392	67.21	65.35	3.45
LUMO+3	177*A*	-0.705	73.80	71.85	7.61
LUMO+1	175*A*	-1.047	78.60	72.39	0.75
LUMO	174*A*	-1.773	18.31	17.58	77.20
HOMO	173*A*	-4.651	33.20	29.88	52.63
HOMO-1	172*A*	-5.126	14.02	13.23	2.27
HOMO-2	171*A*	-5.220	7.82	4.04	0.00
HOMO-5	168*A*	-5.487	12.02	10.22	0.00
HOMO-6	167*A*	-5.562	15.49	14.95	0.70

Discussion and Conclusions

The main finding for end-on $Cp^*_2Sc(\mu\text{-}\eta^1\text{:}\eta^1\text{-}N_2)ScCp^*_2$, **1**, complex is that DFT suggests that its ground state is best described as a triplet. This state assignment is based on the relative energies of different spin states, the agreement between calculated structural parameters and X-ray data, and a comparison between simulated and collected UV spectra. Consistent with the existing literature on these compounds, the two-electron four-center $Sc(d_\pi)\text{-}N_2(\pi^*)$ bonding interactions are evident in the $Cp^*_2Sc(\mu\text{-}\eta^1\text{:}\eta^1\text{-}N_2)ScCp^*_2$ complex. These bonding features, together with the rather large HOMO-LUMO gaps, may explain the intense transitions observed in both the simulated and the collected UV-Vis spectra.

In addition, the DFT findings reveal that the hypothetical side-on $[(Cp^*)_2Sc]_2(\mu\text{-}\eta^2\text{:}\eta^2\text{-}N_2)$ is higher in energy than the synthesized end-on $Cp^*_2Sc(\mu\text{-}\eta^1\text{:}\eta^1\text{-}N_2)ScCp^*_2$ by 0.415 eV (9.57 kcal/mol). For Sc_2N_2, the energy difference between the two binding modes is close to the 12 kcal/mol value previously reported for the first example of an end-on dinitrogen $\{[(R_2N)_3Sc]_2[\mu\text{-}\eta_1\text{:}\eta_1\text{-}N_2]\}^{-2}$ complex.[35] The preferred end-on binding mode of **1** complex is likely due to steric effects that have been previously discussed in many different reduced N_2 rare-earth complexes.[36–40]

Given the isolation of $(N_2)^{3-}$ complexes,[33] the doublet anion models of end-on Sc_2N_2 was investigated. DFT reveals that the $(N_2)^{3-}$ in $\{Cp^*_2Sc(\mu\text{-}\eta^1\text{:}\eta^1\text{-}N_2)ScCp^*_2\}^-$ species are stable only in the presence of polar solvents such as THF. In the gas phase, the frontier HOMOs of these anions are not bound, in contrast to the end-on $(N_2)^{2-}$ compounds which are both stable even in the gas phase. The LUMO of the end-on compounds, as shown in Figure S17, are not localized on the bridge similar to the $[(Me_3Si)_2N]_2(THF)Y_2(\mu\text{-}\eta_2\text{:}\eta_2\text{-}N_2)$ species[33], which can accept one more electron to stabilize a $(N_2)^{3-}$ entity. This may explain why it was not possible to reduce **1** compound further.

Based on the energy of different spin states and selected structural parameters, it appears that closed-shell singlet states are the ground states of the side-on **2** and **3** molecular complexes. This is further corroborated by comparing their simulated electronic spectra with the experimental data to verify the singlet states as the correct ground spin states. The HOMO of **2**, Figure S25 and, **3**, Figure S30, show $Sc(d_\pi)\text{-}N_2(\pi^*)$ bonding as supported by the electronic transitions and population analyses. In **2**, there are two of the two-electron four-center bonding features, with the scandium metal in the center contributing to each of the $Sc(d_\pi)\text{-}N_2(\pi^*)$ bonds. The summary of important excitations is reported above.

In summary, DFT calculations were performed to determine the ground state of the reduced N_2 scandium metallocene complexes. The DFT and TDDFT results were compared with the experimental measurements for validation. Taken together, the DFT calculations suggest that the ground-state of each of the **2** and **3** is best described as a singlet state (S=0), while a triplet state (S=1) is predicted for the **1**. The DFT calculations also revealed the strong covalent interactions due to $Sc(d_\pi)\text{-}N_2(\pi^*)$ bonding in the **1**, **2**, and **3** supported by the electronic transitions and population analyses. The isolated end-on $Cp^*_2Sc(\mu\text{-}\eta^1\text{:}\eta^1\text{-}N_2)ScCp^*_2$ reported in this study is the first neutral end-on Sc_2N_2 complex.

References

1. A. B. Pangborn, M. A, Giardello, R. H. Grubbs, R. K. Rosen, and F. J. Timmers, *Organometallics*, 1996, **15**, 1518-1520.

2. G. R. Fulmer, A. J. M. Miller, N. H. Sherden, H. E. Gottlieb, A. Nudelman, B. M. Stoltz, J. E. Bercaw, and K. I. Goldberg, *Organometallics*, 2010, **29**, 2176-2179.

3. D. F. Evans. *J. Chem. Soc.*, 1959, 2003-2005.

4. S. K. Sur, *J. Magn. Reson.*, 1989, **82**, 169-173

5. G. A. Bain, J. F. Berry, *J. Chem. Educ.* 2008, **85**, 532.

6. C. R. Stennett, J. Q. Nguyen, J. W. Ziller, and W. J. Evans, *Organometallics*, 2023, **42**, 696–707.

7. D. E. Bergbreiter and J. M. Killough. *J. Am. Chem. Soc.*, 1978, **100**, 2126-2134.

8. M.E. Thompson, S. M. Baxter, A. R. Bulls, B. J. Burger, M. C. Nolan, B. D. Santarsiero, W. P. Schaefer, and J. E. Bercaw, *J. Am. Chem. Soc.*, 1987, **109**, 203-219.

9. J. D. Queen, L. M. Anderson-Sanchez, C. R. Stennett, A. Rajabi, J. W. Ziller, F. Furche, and W. J. Evans, *J. Am. Chem. Soc.*, 2024, **146**, 3279-3292.

10. W. Huynh, D. B. Culver, H. Tafazolian, and M. P. Conley, *Dalton Trans.*, 2018, **47**, 13063-13071.

11. APEX2 Version 2014.11-0, Bruker AXS, Inc.; Madison, WI 2014.

12. SAINT Version 8.34a, Bruker AXS, Inc.; Madison, WI 2013.

13. G. M. Sheldrick, SADABS, Version 2014/5, Bruker AXS, Inc.; Madison, WI 2014.

14. G. M. Sheldrick, SHELXTL, Version 2014/7, Bruker AXS, Inc.; Madison, WI 2014.

15. International Tables for Crystallography 1992, Vol. C., Dordrecht: Kluwer Academic Publishers.

16. S. Parsons, H. X. Flack, and T. Wagner, *Acta Cryst. B*., 2013, **69**, 249-259.

17. APEX3 Version 2018.1-0, Bruker AXS, Inc.; Madison, WI 2018.

18. V. N.Staroverov, G. E. Scuseria, J. Tao, J. P. Perdew, *J. Chem. Phys.*, 2003, **119**, 12129–12137.

19. M. K. Armbruster, F. Weigend, C. van Wüllen, and W. Klopper, *Phys. Chem. Chem. Phys.*, 2008, **10**, 1748–1756.

20. S. Grimme, J. Antony, S. Ehrlich, and H. Krieg, H. *J. Chem. Phys.*, 2010, **132**, 154104.

21. S. Grimme, S. Ehrlich, and L. Goerigk, *J. Comput. Chem.*, 2011, **32**, 1456–1465.

22. K. Eichkorn, O. Treutler, H. Öhm, M. Häser, and R. Ahlrichs, *Chem. Phys. Lett.*, 1995, **240**, 283–290.

23. A. Schäfer, H. Horn, and R. Ahlrichs, *J. Chem. Phys.*, 1992, **97**, 2571–2577.

24. F. Weigend and R. Ahlrichs, R. *Phys. Chem. Chem. Phys.*, 2005, **7**, 3297–3305.

25. R. Gulde, P. Pollak, and F. Weigend, *J. Chem. Theory Comput.*, 2012, **8**, 4062–4068.

26. O. Treutler and R. Ahlrichs, *J. Chem. Phys.*, 1995, **102**, 346–354.

27. P. Deglmann, K. May, F. Furche, and R. Ahlrichs, *Chem. Phys. Lett.*, 2004, **384**, 103–107.

28. A. Klamt and G. Schüürmann, *J. Chem. Soc., Perkin Trans. 2*, 1993, 799–805.

29. F. Furche, B. T. Krull, B. D. Nguyen, and J. Kwon, *J. Chem. Phys.*, 2016, **144**, 174105.

30. A. Rajabi, R, Grotjahn, D. Rappoport, and F. Furche, *Dalton Trans.*, 2024, **53**, 410–417.

31. Y. J. Franzke, C. Holzer, J. H. Andersen, T. Begušić, F. Bruder, S. Coriani, F. Della Sala, E. Fabiano, D. A. Fedotov, S. Fürst, S. Gillhuber, R. Grotjahn, M. Kaupp, M. Kehry, M. Krstić, F. Mack, S. Majumdar, B. D. Nguyen, S. M. Parker, F. Pauly, A. Pausch, E. Perlt, G. S. Phun, A. Rajabi, D. Rappoport, B. Samal, T. Schrader, M. Sharma, E. Tapavicza, R. T. Treß, V. Voora, A. Wodyński, J. M. Yu, B. Zerulla, F. Furche, C. Hattig, M. Sierka, D. P. Tew, and F. Weigend, *J. Chem. Theory Comput.*, 2023, **19**, 6859–6890.

32. W. Humphrey, A. Dalke, and K. Schulten, *J. Mol. Graphics*, 1996, **14**, 33–38.

33. W. J. Evans, M. Fang, G. Zucchi, F. Furche, J. W. Ziller, R. M. Hoekstra, and J. I. Zink, *J. Am. Chem. Soc.*, 2009, **131**, 11195–11202.

34. S. Demir, S. E. Lorenz, M. Fang, F. Furche, G. Meyer, J. W. Ziller, and W. J. Evans, *J. Am. Chem. Soc.*, 2010, **132**, 11151–11158.

35. D. H. Woen, G. P. Chen, J. W. Ziller, T. J. Boyle, F. Furche, and W. J. Evans, *J. Am. Chem. Soc.*, 2017, **139**, 14861–14864.

36. S. Demir, S. E. Lorenz, M. Fang, F. Furche, G. Meyer, J. W. Ziller, and W. J. Evans, *J. Am. Chem. Soc.*, 2010, **132**, 11151–11158.

37. A. J. Ryan, S. G. Balasubramani, J. W. Ziller, F. Furche, and W. J. Evans, *J. Am. Chem. Soc.*, 2020, **142**, 9302–9313.

38. J. K. Peterson, M. R. MacDonald, J. W. Ziller, and W. J. Evans, *Organometallics,* 2013, **32**, 2625–2631.

39. A. B. Chung, D. Rappoport, J. W. Ziller, R. E. Cramer, F. Furche, and W. J. Evans, *J. Am. Chem. Soc.*, 2022, **144**, 17064–17074.

40. N. Ouddaï, K. Costuas, M. Bencharif, J.-Y. Saillard, and J.-F. Halet, *Comptes Rendus Chimie*, 2005, **8**, 1336–1350.